

# Directed self-assembly of chiral liquid crystals into biomimetic bouligand structures in thin film

Received: 24 February 2025

Accepted: 15 September 2025

Published online: 21 October 2025

 Check for updates

Tejal Pawale<sup>1</sup>, Justin Swain<sup>2</sup>, Mesonma Anwasi<sup>1</sup>, Sachin Kaluarachchi<sup>3</sup>, Yuheng Wang<sup>1</sup>, Yong Yang<sup>3</sup>, David A. Czaplowski<sup>4</sup>, Ralu Divan<sup>4</sup>, Giordano Tierra<sup>2</sup> & Xiao Li<sup>1</sup>✉

The Bouligand structure, renowned for its helicoidal arrangement and enhanced mechanical properties, has attracted significant research interest for its ability to impart enhanced strength to intrinsically soft materials. Biomimetic approaches have centered on fibrous structures in bulk materials, but translating this architecture into thin-film regime for miniaturized-wearable devices with programmable functions remains challenging. Here, we direct the self-assembly of cholesteric liquid crystals (CLCs) into hierarchical helical structures using chemically patterned surfaces. Alternating surface anchoring regions align uniform lying-down helices at the nanoscale, guiding a secondary microscale helical structure exhibiting both left- and right-handed twists. This mimetic Bouligand structure in CLCs enables optical modulation under applied field and strain with enhanced mechanical response. Simulations reveal the structural evolution from initial Bouligand configuration in LC layers to alternating twist helices. This research provides a basis for designing and manufacturing miniaturized or wearable devices with nanometer-scale precision in regulating electro-optical and mechanical properties.

Miniaturized devices have become one of the fastest-growing technology markets and are rapidly evolving in functionality, size, and application scope, impacting every aspect of daily life, including wearable healthcare devices, soft robotics, flexible displays, and sensors<sup>1–8</sup>. Scaling down to the micrometer level, integrating multiple functions, and simultaneously enhancing performance with high efficiency place stringent demands on material design and manufacturing<sup>1,8</sup>. More specifically, material characteristics such as mechanical integrity, optical sensitivity, durability, and environmental stability are essential to the overall performance of miniaturized devices and remain significant challenges when scaling down to the mesoscale. Traditional materials for miniaturized devices, including metals, semiconductors, ceramics, and polymers, are well-known for their excellent electrical properties and optical performance<sup>6,9–11</sup>.

Nevertheless, the components' inherent lack of flexibility, stretchability, and processing capabilities significantly challenge applications in flexible devices, which explicitly require high adaptability and stretchability. Innovative assembly techniques, such as hybrid material integration, flexible printing methods, and strain-engineered structures, are employed<sup>10–14</sup> to achieve mechanical enhancements without sacrificing sensitivity, which could unlock great potential for expanding miniaturized devices in diverse fields such as foldable displays, wearable sensors, and artificial skins. Soft materials, such as polymers and elastomers, offer excellent flexibility due to the elasticity of macromolecules but exhibit weak mechanical properties due to their intrinsic light elements and bond energy. Combining organic and inorganic materials, such as integrating nanowires or nanoparticles into a polymer base, offers mechanical robustness without sacrificing

<sup>1</sup>Materials Science and Engineering Department, University of North Texas, 3940 North Elm Str, Denton, TX, USA. <sup>2</sup>Department of Mathematics, University of North Texas, 1155 Union Circle, Denton, TX, USA. <sup>3</sup>Department of Biomedical Engineering, University of North Texas, 3940 North Elm Str, Denton, TX, USA.

<sup>4</sup>Center for Nanoscale Materials, Argonne National Laboratory, Lemont, Illinois 60439, USA. ✉e-mail: [Xiao.Li@unt.edu](mailto:Xiao.Li@unt.edu)

flexibility<sup>15,16</sup>. However, long-term stability is often compromised by fracture and creep due to the large modulus mismatch between soft and rigid materials<sup>17,18</sup>.

Addressing the mechanical limitations of soft materials without relying on traditional inorganic materials can be achieved by turning to nature, which has evolved over millions of years to provide solutions based on efficient material microstructure design. In numerous biological materials, such as mantis shrimp dactyl clubs<sup>19</sup> and beetle exoskeletons<sup>20,21</sup>, the Bouligand microstructure, with its naturally occurring periodic helical pattern, has demonstrated notable mechanical properties<sup>19,20,22,23</sup>, along with vivid colors, emerging as a focal point for advanced material design. The hierarchical assembly of lightweight yet ductile building blocks, such as fibers of collagen or chitin, creates a material with significant damage tolerance and strength, comparable even to tough brick-and-mortar materials<sup>24–26</sup>. The structure is designed to achieve efficient stress transfer and energy dissipation through the rotation and reorientation of nanofibers under external load<sup>27</sup>. In addition, the higher-order arrangement inherently limits crack propagation and contributes to enhanced toughness. The distinct mechanical resilience of the Bouligand structure has inspired the creation of functional materials that replicate its structural organization. Among these, cellulose nanocrystals (CNCs) stand out as the most studied system, highly regarded for their ability to self-assemble into chiral structures. Research has primarily focused on CNC-based composites that can self-organize into Bouligand structures, resulting in bulk materials with significant strength. Conventional approaches typically emphasize the generation of large-area uniform Bouligand structures<sup>28–30</sup>, which cannot achieve the necessary precision and consistency required for miniaturized design. Especially, to advance biomimetic Bouligand structures into modern applications, strategies need to be developed to create high-precision, scalable and position-dependent structures. Most importantly, the underlying physics principles driving the structure formation and the structure-property relationship between the Bouligand structure and impact resistance remain largely unknown or underexplored.

Considering the smaller length scale of liquid crystal (LC) molecules, the helicoidal and heliconical organization found in chiral and achiral LC phases provide a route for biomimicking the Bouligand structure and unveiling structure-property relationships. In both phases, molecules rotate around the helical axis; in the heliconical structure, they rotate at an oblique angle, in contrast to the perpendicular rotation in the helicoidal structure. A complete 360° rotation of the director along the helical axis defines the pitch  $p$  of the chiral materials. Crucially, while CNCs of ~200–300 nm in length can assemble chiral structures on the scale of a few hundred nanometers, the much smaller LC molecules (~1–2 nm) can organize into helices with even finer pitches, further enhancing the hierarchical nature of these structures. The intrinsic responsive nature of LCs allows precise control of nanoscale interactions, enabling the creation of highly organized microscale features through the use of a substrate with topographic features or chemical patterns. The technique, known as directed self-assembly, exploits the natural tendencies of soft materials to achieve self-organized, well-ordered morphologies that are typically unavailable through conventional methods<sup>31–34</sup>. We have previously used chemically patterned surfaces to direct the self-assembly of blue phase liquid crystals into single crystals with selective lattice orientation<sup>35</sup>. Building upon this, in this work, we use chemically patterned surfaces to direct the assembly of highly chiral nematic liquid crystals into hierarchical helical structures. Recently, several groups have explored the use of anchoring patterns to control the formation of blue phases (BPs). For instance, Nakajima et al. applied one-dimensional photoalignment patterning on the substrate to induce a slanted BPII lattice. Liu et al. demonstrated that striped photoaligned surfaces could stabilize monodomain BPs structures, combining experimental studies with Landau–de Gennes (LdG)

simulations to guide BPs unit cell orientation<sup>36,37</sup>. Similarly, Emeršič et al. employed chemically patterned substrates to direct BPs self-assembly, with complementary LdG modeling to optimize the pattern design<sup>38</sup>. While these efforts focus on BPs systems characterized by cubic lattices and double-twist cylinders, our work turns to the cholesteric phase, which exhibits fundamentally different structural motifs. In this work, the chemically patterned surface directs the self-assembly of Bouligand-type helicoidal architectures, which evolve into secondary microscale helical structures with alternating left- and right-handed twist domains, rather than BPs disclination networks.

Inspired by the natural Bouligand structure, to address the mechanical limitations of soft materials, the highly chiral cholesteric phase of liquid crystals is confined as a thin film between the nanoscale chemically patterned bottom substrate and a liquid crystalline polymer brush-modified top substrate. We assemble a microscale helical structure aligned perpendicular to the stripe length of the chemical pattern and exhibiting periodic left- and right-handed twists. The hierarchical nature of the morphology enables the integration of mechanical reinforcement and photonic band gap modulation. Additionally, we manipulate the top substrate anchoring, the space of confinement, and the chemical pattern dimension to control the periodicity of the helical structure, the length of the helices, and the number of hierarchical layers. We present a system capable of efficiently and precisely controlling the location, nanoscale size, and scalability of a hierarchical structure analogous in nature to the Bouligand structure. Importantly, the tunable chemically patterned surfaces with dimension, geometry, and chemical contrast provide an integrated platform to reveal the underlying physics principles driving the structure formation and the structure-property relationship between Bouligand structure and impact resistance, which remains largely unknown or underexplored in science and technology. Simulations based on the Landau–de Gennes Q-tensor model, designed to replicate the Bouligand architecture by rotating stacked layers of LC helices  $\pm 45^\circ$ , reveal three-dimensional periodic arrangements and visualize disclination lines. These 3D director maps, combined with confocal fluorescence microscopy, confirm the hierarchical structure formation throughout the film thickness. Further, tensile testing of films reveals anisotropic and reversible strain responses, while the application of an electric field produces a reversible optical modulation. Together, these results demonstrate a platform for creating scalable, defect-engineered, tunable soft photonic structures. Our work represents a class of chemical pattern-induced chiral organization in cholesteric systems, offering a soft-matter analogue to Bouligand-type biological architectures in the thin film regime. It opens an avenue for designing chiral structural LC-based miniaturized devices to overcome limitations of soft materials for programmable optical/mechanical properties, and supports development of wearable devices, artificial skin, and sensors.

## Results

A highly chiral solution, capable of transitioning into blue phase liquid crystals, was prepared by doping the nematic host MLC2142 with left-handed chiral dopant S811 (36.32 wt%) (Fig. 1a). The solution exhibited the following phase transitions: cholesteric phase to BPI at 41 °C; BPI to BPII at 42 °C, and BPII to isotropic at 44 °C. In the cholesteric phase, the liquid crystal (LC) director is twisted along a single axis, while twists in all directions form double twist cylinders (DTCs), which are the building blocks of blue phase liquid crystals. The arrangement of DTCs and disclination lines forms a 3D body-centered cubic structure, defined as BPI, followed by a simple cubic structure in BPII. In previous studies, to achieve a BPII single crystal, we relied on a chemical pattern with periodic regions of planar and homeotropic anchoring<sup>35</sup>. Here, chemical patterns were used to investigate the cholesteric phase of the LC, which is usually neglected in high-chirality systems because the chiral pitch is below the visible wavelength range and cannot be

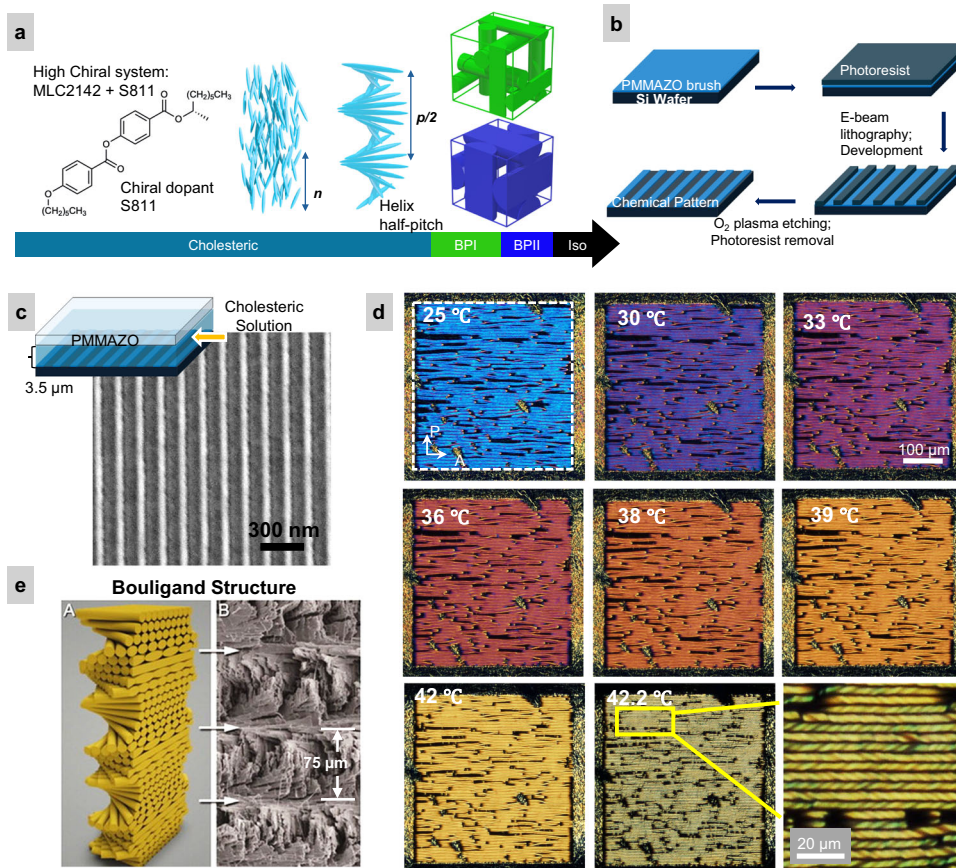


**Fig. 1 | Engineering the hierarchical helical morphology using directed self-assembly.** **a** Nematic liquid crystal (LC) host (MLC2142) and chiral dopant (S811) for cholesteric phase material; chiral nematic LC and the half-pitch of the helix; double-twist cylinder and unit cell structures of BPI (top) and BPII (bottom). **b** Fabrication scheme for chemical patterns on a silicon substrate. **c** Scanning electron microscopy (SEM) images of a patterned silicon substrate; cholesteric phase material confined between a PMMAZO-coated top glass (weak homeotropic anchoring) and a chemically patterned substrate (alternating homeotropic and

planar anchoring) with a gap of 3.5  $\mu\text{m}$  via capillary action. **d** Reflection optical microscopy images showing the thermal treatment of the cholesteric phase from room temperature to prior to the BPI transition temperature for the chemically patterned area. **e** Schematic of the Bouligand structure found in nature, along with a scanning electron microscopy image of the Bouligand structure. Reproduced from Weaver, J. C. et al., *Science* 336, (<https://doi.org/10.1126/science.1218764>), AAAS<sup>19</sup>.

directly observed by optical microscopy. The fabrication process of the chemically patterned area is illustrated in Fig. 1b. A clean silicon substrate was uniformly coated with a 0.05 wt% poly(6-(4-methoxyazobenzene-4'-oxy) hexyl methacrylate) (PMMAZO) brush to provide a grafting density of  $2.02 \times 10^{-2}$  chains/nm<sup>2</sup><sup>39</sup>.

Depending on the grafting density of the PMMAZO brush, the LC molecular alignment with respect to the substrate can be controlled. A high grafting density aligns molecules parallel to the surface, while a low grafting density surfaces aligns them almost perpendicular to the substrate. Intermediate grafting densities produce different tilt angles for LC molecules. To create the nanopattern, a PMMA photoresist was deposited on top of the brush and patterned using e-beam lithography. Subsequent exposure and development of the PMMA film opened periodic trenches, exposing the PMMAZO brush (Fig. 1c). Oxygen plasma was then employed to etch the brush, and after photoresist removal, stripes of planar anchoring in a weak homeotropic background were formed. The period of alternating planar-homeotropic anchoring regions is defined as  $P$ , while the widths of planar or homeotropic stripes are defined as  $W_p$  and  $W_h$ , respectively. A 0.05 wt% PMMAZO modified glass as the top surface was used to assemble into a LC cell with a thickness of 3.5  $\mu\text{m}$  as shown in Fig. 1c schematic. The solution was injected into the LC cell via capillary action at isotropic temperature and cooled naturally. In the following experiments, we also varied the PMMAZO grafting density on the top

surface, the chemical pattern dimensions, and cell thickness to study the confined cholesteric phase structure.

### Chemically patterned surfaces directed the hierarchical helix formation

After confining the highly chiral cholesteric phase into an LC cell, the morphological transition from room temperature to prior to the BPI transition point is shown in Fig. 1d. Based on the helical twisting power (HTP) and concentration of dopant, the intrinsic pitch of cholesteric phase is calculated to be 290 nm. Such small helix pitch makes randomly oriented cholesteric liquid crystals (CLCs) outside the patterned field to show no obvious helical features, but only random colors (Supplementary Fig. 1). In contrast, inside the chemical pattern area, dominant lines aligned perpendicular to the stripe length are observed and measured to be 7.8  $\mu\text{m}$  in width and cover the entire patterned region. The assembled stripes reflect different colors with increasing temperature. The helical twisting power of chiral dopant S811 is sensitive to temperature, modulating the pitch of the cholesteric phase by the change of thermal energy. The selective reflection of light along the helix axis when the wavelength matches the pitch of CLC is given as  $\lambda = n \cdot p \cos\theta$ , where  $n$  (refractive index) is the average of ordinary and extraordinary indices and  $\theta$  is the angle between the light propagation direction and the helix axis. Therefore, the changes in temperature cause shifts in reflective color of the morphology.

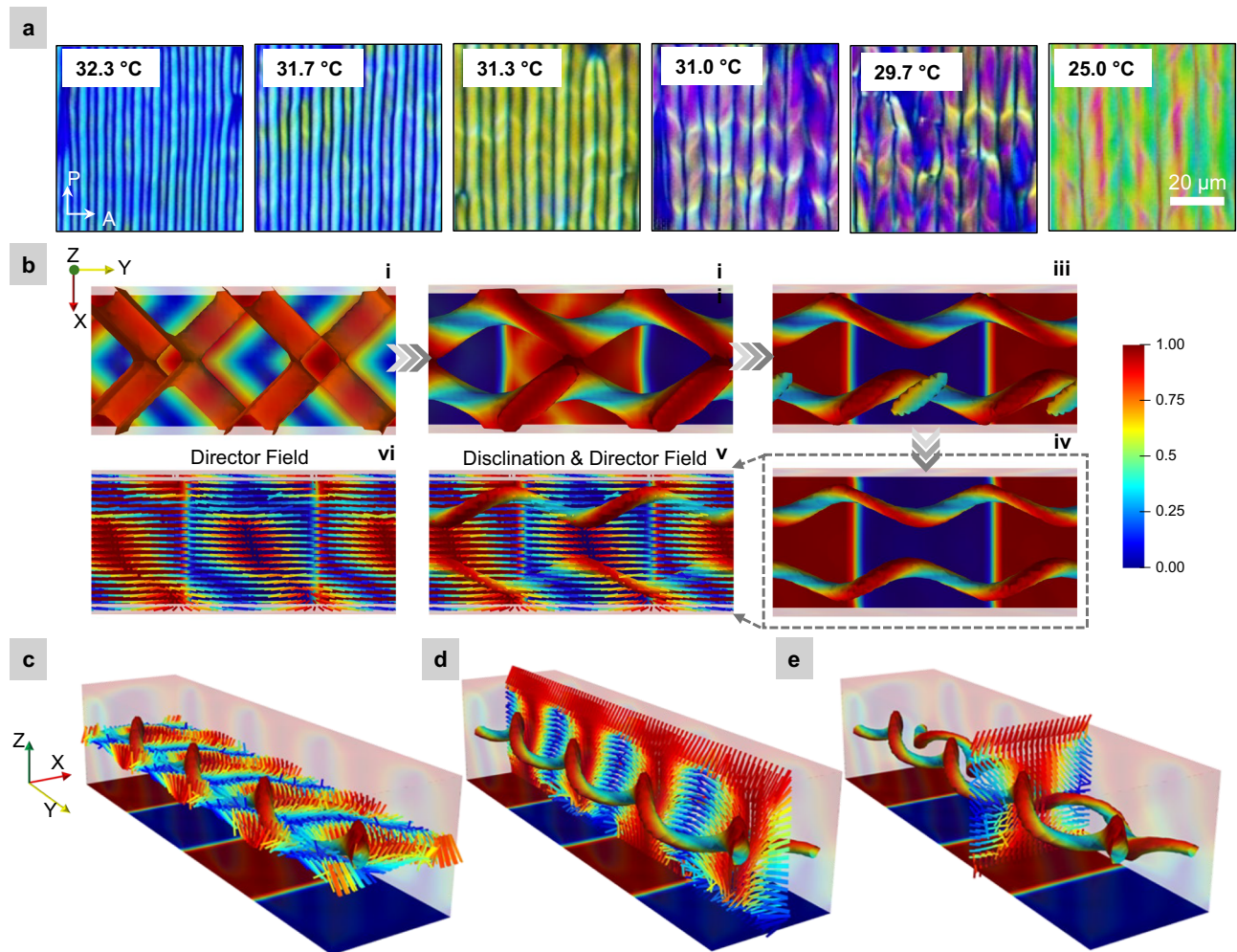


**Fig. 2 | Evolution of the hierarchical helical morphology.** **a** Polarized optical microscopy images of the cholesteric phase after the phase transition from BPI to room temperature. Scale bar: 10  $\mu\text{m}$ . Simulations showing the evolution of the helical structure from the cholesteric phase, assembled similarly to the Bouligand architecture. **b** Top-down view of simulation results: Snapshots are taken at  $t = 0$  (i),  $2.5e-4$  (ii),  $5e-3$  (iii), and  $1e-1$  (iv). For stabilized morphology in iv, simulation showing director field and disclination lines superimposed (v), and director field

alone (vi). **c–e** Cross-sectional views of the stabilized morphology showing disclination lines and director orientation in a 3D cell across the c) x-y, d) y-z, and e) x-z planes. In simulations, the isosurface is shown using  $|Q|^2$ , which measures the degree of orientation, and represents the disclination lines in the material. The color scale measures the alignment of the orientation of the molecules with respect to the z-axis, where value 0 (blue) corresponds to orthogonal alignment, and value 1 (red) parallel alignment.

However, it is important to note that outside the chemical patterned area, this pitch shift does not influence the visible characteristics of the as-assembled CLCs. Near the cholesteric-BPI transition, we observed the lines transforming into a helical morphology that twisted periodically to the left and right over the patterned area. The width of the rope-like texture banded with left- and right-handed twist, is indicated as periodic and is around  $8.5 \mu\text{m}$ . Whereas the pitch of the helical morphology, defined as full  $360^\circ$  rotation (for both left- and right-handed helices), is  $-7.4 \mu\text{m}$  (highlighted in Fig. 1d zoomed in image). Such alternating twisted helix structure appears more obvious when a half-wave retardation plate is used in the POM images (Supplementary Fig. 2). Considering the intrinsic  $-290 \text{ nm}$  pitch structure in the cholesteric phase and the  $150 \text{ nm}$  period of the chemical pattern, it is notable that the nanoscale pattern stabilized the cholesteric phase morphology into a microscale helix that exceeded its natural pitch value. We refer to this microscale helix assembly from a nanoscale pitch cholesteric phase, exhibiting both left-handed and right-handed twists, as a hierarchical helical (HH) structure. This hierarchical helical structure, formed on top of the chemical pattern, shows similarity to the order observed in the Bouligand structure (Fig. 1e), which is usually composed of layers of chitin or collagen fibers stacked in a highly

ordered, twisted arrangement. Each layer of fibers aligns parallel to the plane and each layer rotates incrementally with respect to the adjacent layer around a central axis. A full  $360^\circ$  rotation over several layers of fibers generates a hierarchical, helicoidal pattern. While the periodicity of the helicoidal ordering observed in natural systems varies from nanoscale to macroscale, similar to the Bouligand architecture, the LC molecules in our system organize into larger, ordered structures via interaction at the nanoscale to create a microscale helical order.

#### Phase transition and temperature-dependent helix structure

Thermotropic LCs undergo phase transitions and characteristic changes when thermal energy is applied, including pitch modulation of the cholesteric phase. The morphological transition experienced by the hierarchical helical structure of the Chol. phase in response to temperature changes was monitored at a slower cooling rate of  $0.1^\circ\text{C}$  per minute. First, the system was cooled from the isotropic phase to BPI, and the morphological evolution after the BPI-Chol. phase transition was recorded as a series of POM images, shown in Fig. 2a. During the cooling cycle, the phase transition temperature from BPI to cholesteric phase was noted to be around  $32.3^\circ\text{C}$ . At the molecular level, this transition can be explained by LC molecules changing from being

twisted along all directions in the blue phases to being twisted along a single axis in the Chol. phase. Macroscopically, this change was observed as dark and bright fringes, commonly referred to as uniform lying-down helices (ULH)<sup>40</sup>. The dark stripes indicated that the LC molecules were oriented perpendicular to the substrate, thus not interacting with light, while the bright fringes appeared when the molecules were tilted at an angle, reflecting light. The helical axis of the ULH aligned along the length of the chemical pattern stripes, consistent with previous studies demonstrating ULH director alignment along the rubbing direction<sup>41,42</sup>. The pitch of lying-down helices at this point was measured to be around 3.7  $\mu\text{m}$ . As the temperature dropped to 31.3 °C, a gradual twist along the bright fringes of the ULH was detected, accompanied by a slight change in the reflective color from cyan blue to yellow. The periodicity of the helices increased accordingly to 5.1  $\mu\text{m}$ . Further cooling shifted the reflective color to bright pink, with the helix period measuring 5.8  $\mu\text{m}$  at 31.0 °C. At 29.7 °C, the lying-down helices transformed into a twisted, rope-like structure with a period of 6.4  $\mu\text{m}$ , which remained stable down to room temperature. The helical axis of this ribbon-like twisted structure was oriented orthogonally to the helical axes of the ULH. The gradual increase in the periodicity of the helix with decreasing temperature is plotted as a function of temperature in Supplementary Fig. 3. The morphological transition from ULH to the twisted, rope-like structure further supports this configuration as a hierarchical assembly.

To test the theory that a Bouligand-like organization of the cholesteric structure in liquid crystal phase results in the formation of the hierarchical helical structure observed we performed numerical simulations. The Landau-de Gennes Q-tensor model was used, which represents the average local orientation of the molecular director using the eigenvectors of a second-order tensor. In the particular case of neglecting the hydrodynamics effects in the model, it can be viewed as a gradient flow of an energy functional, which includes an additional term in the elastic energy to describe the effect of long range director twisting present in high chiral systems using a twisting parameter,  $q_0$ , that is inversely proportional to the helical pitch  $p = 290 \text{ nm}$ . With this model, we approximate the dynamics of the liquid crystal material when the hydrodynamic effects are negligible, as the system moves from high to low energy by balancing elastic and thermotropic energy contributions. In Fig. 2b, we show the dynamics of an opposite-twist helical structure formation, subjected to chemically patterned boundary conditions on the lower surface, and weak homeotropic anchoring on the top. It should also be noted that we use periodic boundary conditions in both the  $x$  and  $y$  directions, which in the  $y$ -direction represents infinitely long helices, and in the  $x$ -direction represents that the helices are flanked by another pair of two at each side, which resembles the column arrays of alternating twist helices observed in experiments, which is necessary to stabilize these structures.

The initial conditions are two distinct layers of helices, which are aligned in perpendicular directions to each other, so that they give the appearance of a Bouligand-like twisting structure and are then mirrored across the  $y$ -axis (Supplementary Fig. 4). As the simulation evolves, the initially stacked layers resembling a Bouligand-like twist gradually smooth into a continuous arrangement of rope-like helices with alternating handedness (Fig. 2b.i-iv). This structural transition is first observed through the emergence of disclination lines at the boundaries between domains, where the intrinsic cholesteric twist is incompatible with the imposed surface alignment. These disclination lines mark regions of high elastic distortion and indicate areas where the director field cannot be smoothly accommodated. To visualize these features, iso-surfaces of the scalar order parameter  $|\mathbf{Q}|^2$  are used, which highlight the locations of reduced orientational order corresponding to disclination lines. In subsequent visualizations, we overlay the director field onto the stabilized structure to further clarify how these disclination lines relate to the surrounding molecular orientation

(Fig. 2b.v). The corresponding director field of the fully developed morphology is also shown in Fig. 2b.vi. Together, these simulations capture the formation pathway of the hierarchical helical morphology and its internal topological features under confinement. The color scale indicates the alignment of the director with respect to the vertical  $z$ -axis, and the alternating red-blue pattern on the helix shows that the director is twisting around the helix.

To further elucidate the 3D organization of the morphology, we present simulated director fields and disclination lines within confined LC cells at different planes. In Fig. 2c, the  $XY$  plane visualization shows periodic cholesteric helices aligned predominantly along the  $Y$  direction, consistent with the surface patterning. However, the orientation gradually shifts along the  $X$ -axis, leading to the formation of repeating domains with phase-offset helices. This shift generates lateral modulation in the director field, which mirrors the periodic stripe textures seen in POM. In the  $YZ$  plane (Fig. 2d), the director field exhibits strong long-range order along the  $Y$  direction, extending throughout the cell thickness ( $Z$ -axis). However, the helical orientation gradually shifts as one moves vertically through  $Z$ , indicating a vertical modulation of the pitch axis. This reflects a continuous rotation of the helix with depth, consistent with layered twist propagation and domain evolution. In the  $XZ$  plane (Fig. 2e), the cholesteric helices are observed to reorient and curve along the  $X$  direction, while showing alternating domains separated by regions of homeotropic alignment. This spatial variation of the director with depth illustrates how the helicoidal axis tilts and curves through the cell, producing curved domains due to competing anchoring and intrinsic twist. The observed periodicity and bending suggest oblique modulation of the cholesteric structure along  $Z$ . The morphology is best described as a three-dimensionally modulated helicoidal structure, composed of periodic, chiral domains organized across all spatial directions. Planar stripe domains ( $XY$ ) emerge from lateral pitch shifts, continuous helicoidal layers form along the vertical ( $YZ$ ) axis, and oblique, rope-like helices appear in the  $XZ$  plane due to twist frustration and confinement. Together, these features create a hierarchical helix-within-helix arrangement characteristic of the observed structure.

### Interlayer rotation of microscale helices observed through confocal microscopy

To investigate the cholesteric layer arrangement that leads to the hierarchical structure, we performed confocal laser scanning microscopy. A 6  $\mu\text{m}$  thin cholesteric liquid crystal film, doped with the fluorescent dye Nile Red, was prepared and subsequently polymerized to lock in the hierarchical helical (HH) morphology. The Nile Red molecules align along the local director, allowing selective visualization of orientation differences. After polymer stabilization, the sample was examined with laser scanning confocal microscopy in transmission mode, which provided high-resolution optical sections in the  $XY$ ,  $YZ$ , and  $XZ$  planes. Since Nile Red fluoresces most strongly when its dipole is perpendicular to the optical axis, intensity variations directly reflect local director orientation. In the control sample without any substrate patterning (Fig. 3a), the  $XY$  confocal slice reveals a disordered cholesteric morphology characterized by irregular but periodic intensity modulations, indicative of local variations in helical axis orientation. The  $XZ$  cross-section lacks discernible order, consistent with random in-plane helix orientation and limited vertical coherence. In contrast, the  $YZ$  slice exhibits periodic intensity bands aligned orthogonal to the  $Y$ -direction and continuous along the  $Z$ -direction, reflecting vertically aligned cholesteric layers with a uniform helical pitch. From this regular spacing, the pitch is estimated to be  $456 \pm 20.4 \text{ nm}$ . The deviated pitch from the cholesteric solution can be attributed to the limited axial resolution of confocal microscopy, as well as the projection and possible overlap of multiple helicoidal layers across the film thickness.

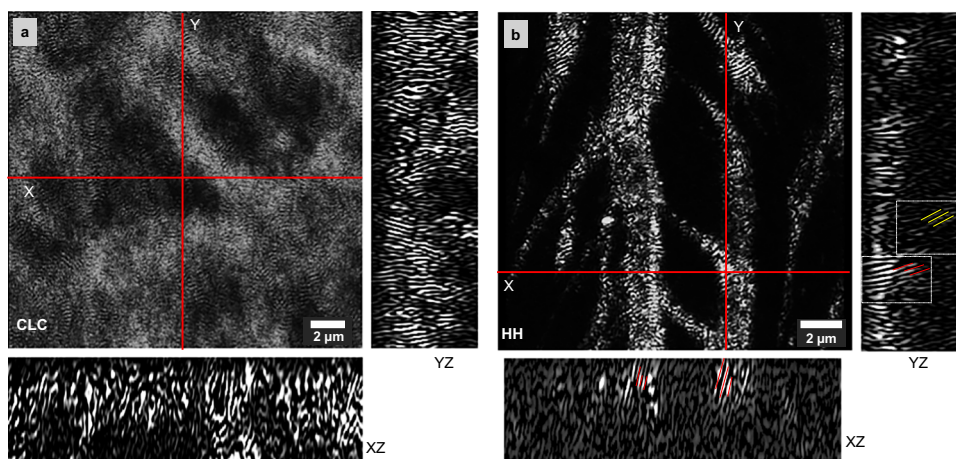


**Fig. 3 | Confocal fluorescence microscopy of cholesteric (CLC) and hierarchical helical (HH) morphologies.** Confocal XY images are shown with red crosshairs indicating the positions of the extracted orthogonal slices. The YZ slice is displayed

to the right of each XY image, and the XZ slice is shown below. **a** Confocal slices of polymerized CLC film showing uniform planar alignment. **b** Confocal slices of HH morphology showing multilayered twisted structure.

In contrast, the XY confocal 3D profile image of the HH sample displayed in Fig. 3b reveals a well-organized network of bright bands, primarily aligned vertically but interspersed with diagonally oriented domains. Consistent with optical and simulation results, these features correspond to the hierarchical arrangement of helices, where enhanced fluorescence arises from regions with favorable director orientation relative to the excitation beam. To better resolve the 3D structure, orthogonal slices (YZ and XZ) were extracted along the red crosshairs in the XY plane. In the YZ confocal slice, the bright bands associated with regions of out of plane director orientation exhibit a gradual vortical shift along Z as one moves across the Y-direction. This angular deviation suggests that the pitch axis is not strictly vertical but undergoes lateral curvature. Consistently, the simulated YZ slice in Fig. 2d shows a comparable modulation in the director field, where the apparent position of the cholesteric bands shifts vertically (along Z) as one moves laterally across Y. This spatial variation observed in both experiment and simulation confirms the presence of nonuniform, laterally curved helicoidal domains indicative of hierarchical organization. In the XZ confocal slice extracted along the marked line in the XY plane, periodic bright and dark bands appear diagonally, with the brightest regions aligning with vertical stripes in the XY image. These bands indicate helicoidal domains whose pitch axes lie primarily along the X-direction but exhibit a pronounced curvature through the film thickness (Z-direction), consistent with the simulated morphology showing spatially modulated, oblique cholesteric alignment. The estimated nanoscale pitch of  $487 \pm 18.5$  nm from both XZ and YZ slices confirms the preservation of intrinsic cholesteric periodicity even within the HH morphology. This multiscale structuring likely arises from the interplay between substrate-imposed boundary conditions and intrinsic elastic anisotropy, which collectively drive curvature and reorientation of local pitch axes. Together, the confocal microscopy and simulation results converge to reveal a three-dimensionally modulated helicoidal morphology characterized by twisted, laterally shifting domains and disclination-guided hierarchical organization.

### Polymer brush enables the stabilization of the hierarchical helical morphology

The anchoring energy of the top substrate is critical in stabilizing such metastable structures generated by the cholesteric phase on the chemically patterned region. Although the chemical pattern directs the formation of ULH, the anchoring energy of the top substrate determines whether HH formation is feasible. In the case of strong homeotropic and planar-anchored substrates, the alignment enforced on the LC molecules is perpendicular and parallel to the substrate,

respectively. Therefore, in systems with strong anchoring energies, the hierarchical helical structure does not form over the pattern area. The POM images of both cases are shown in Supplementary Fig. 5a, b. Changing the grafting density of the PMMAZO brush from low to high tunes the orientation of LC molecules from perpendicular to planar. While keeping the chemical pattern dimensions ( $W_P = 150$  nm;  $W_H = 75$  nm) and film thickness ( $3.5 \mu\text{m}$ ) constant, the grafting density of the top substrate was gradually increased from  $1.72 \times 10^{-2}$  chains/ $\text{nm}^2$  (0.025 wt%) to  $9.4 \times 10^{-2}$  chains/ $\text{nm}^2$  (1.0 wt%). Figure 4 schematically illustrates how the grafting density of PMMAZO side-chain mesogens modulates liquid crystal (LC) alignment at the substrate interface. At low grafting density (left), the sparse mesogens adopt an upright orientation due to limited steric hindrance, promoting homeotropic LC alignment. As the grafting density increases (middle), lateral crowding induces a tilt in the mesogen orientation, leading to tilted LC alignment. At high grafting density (right), the dense mesogen packing favors nearly planar anchoring, aligning the LC molecules parallel to the substrate. This progressive shift in alignment with increasing density enables tunable surface anchoring behavior. Thermal-treated POM images from room temperature to the phase transition temperature for low, moderate, and high grafting density conditions are displayed in Fig. 4b–d. At the lowest grafting density of  $1.72 \times 10^{-2}$  chains/ $\text{nm}^2$  (Fig. 4b), the period of the HH structure over the pattern area was  $13.38 \mu\text{m}$ . As grafting density increased to  $2.65 \times 10^{-2}$  chains/ $\text{nm}^2$  (Fig. 4c), the period decreased to  $8.7 \mu\text{m}$ . Further increasing grafting density to  $9.24 \times 10^{-2}$  chains/ $\text{nm}^2$  (Fig. 4d) induced planar alignment, resulting in a morphology with a period of  $10.4 \mu\text{m}$ , which is higher than that of the moderate grafting density. The POM images for the remaining grafting densities and the plot of the structure's periodicity as a function of grafting density are in Supplementary Fig. 6a, b. Regardless of the grafting density, the HH structure was always stabilized over the patterned region. Therefore, we determined that PMMAZO brushes are essential for successfully guiding the assembly of the hierarchical helical structure. The side-chain mesogen along the brush backbone, with free rotation capability and adjustable tilted angles, plays a key role in allowing LC molecules to align in various configurations. This enables the molecules to successfully adapt to and further assemble the uniform lying-down helices, regardless of the thickness and grafting density.

### Dimension of chemical pattern affects helix morphology

The contribution of the chemical pattern is crucial for aligning the director of the helical axis and leading to the formation of a hierarchical helical morphology at different dimensions. Since the pitch of

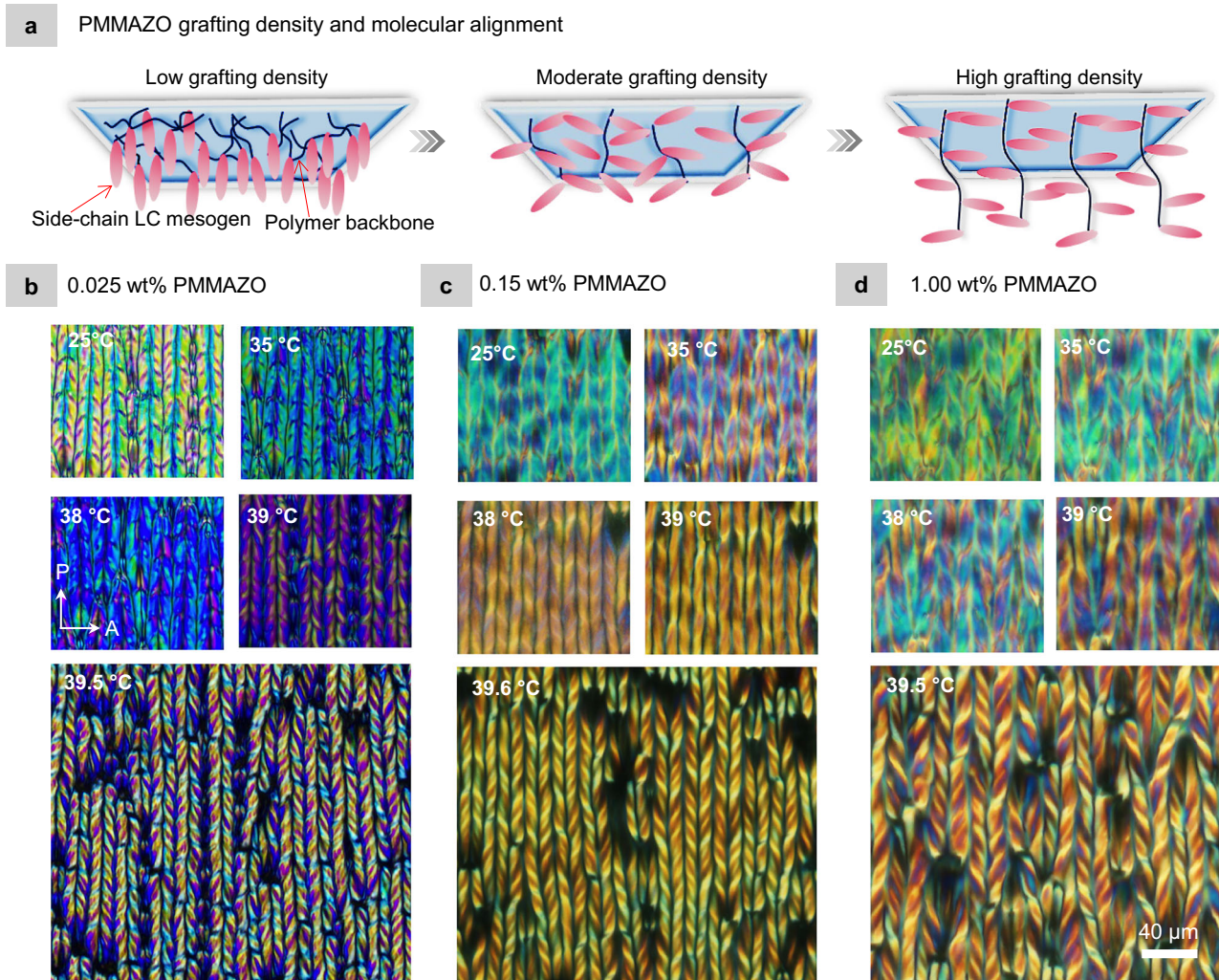


**Fig. 4 | Polymer brush stabilizes the hierarchical helical morphology.** **a** Schematic representation of LC alignment as a function of PMMAZO grafting density. Increasing grafting density alters the orientation of the polymer brush at the substrate-LC interface, leading to distinct alignment configurations of LC molecules: homeotropic, tilted, and planar, respectively. POM images showing the

morphology during heating cycles under different anchoring conditions set by the top substrate. **b**  $1.72 \times 10^{-2}$  chains/nm<sup>2</sup> (0.025 wt% PMMAZO). **c**  $2.65 \times 10^{-2}$  chains/nm<sup>2</sup> (0.15 wt% PMMAZO). **d**  $9.24 \times 10^{-2}$  chains/nm<sup>2</sup> (1.0 wt% PMMAZO). The visible area varies between images to highlight both local and large-scale morphological features; all images are shown at the same magnification; Scale bar: 40  $\mu$ m.

the cholesteric phase is sensitive to the concentration of the chiral dopant, the chemical pattern dimensions should be adjusted accordingly. To understand the effect of pattern dimensions on the hierarchical morphology, the period was fixed at 150 nm, and the widths of planar and homeotropic anchoring regions were varied ( $W_P = 100$  nm;  $W_H = 50$  nm, and vice versa). Other aspects of the sample, such as LC cell thickness and top anchoring energy (0.05 wt% PMMAZO), were kept constant. The period of the morphology was measured to be  $14 \pm 0.5 \mu$ m for both cases. Figure 5a shows optical images of the morphology prior to the phase transition, along with plot of periodicity for each case. The period of the chemical pattern was gradually increased while keeping the widths of homeotropic and planar regions equal. The period of the assembled structure decreased to  $13.6 \mu$ m for a period of 280 nm and to  $13.3 \mu$ m for a period of 300 nm, similar to the chemical pattern with  $P$  of 150 nm and equal stripe widths. However, further increasing the period to 450 nm significantly reduced the structure's period to  $11.7 \mu$ m. To understand the morphological tolerance of the chemical pattern to HH structure at larger periods,  $W_P$  was set to 75 nm, and the period was varied from 375 nm to 525 nm. For a 375 nm period, the morphology period was measured at  $9.09 \mu$ m, and for 525 nm, it was  $10.6 \mu$ m. The sudden increase in periodicity of the HH

structure, especially on the surface of patterns with larger periods, was caused by multiple deformation regions, resulting in distorted morphology. These variations in pattern dimensions also influenced the length of the hierarchical helical structure domains. Disruption in molecular alignment creates a break in the continuous formation of the HH morphology. Thus, we define the domain length as the length over which the HH structure forms continuously. Figure 5b show the use of a chemically patterned area of  $440 \mu$ m  $\times$   $440 \mu$ m with a period of 280 nm and  $W_P/W_H$  of 140 nm to direct the assembly of hierarchical helical structure. The regions marked with white dashed boxes indicate the domain length of the HH structure, as defined earlier. In this case, the average domain length was around  $150 \mu$ m, which is smaller than the 150 nm period and larger than the 300 nm period. The domain length for each case was measured, averaged, and plotted against the pattern dimension. However, further differences in cholesteric phase pitch and pattern period substantially reduced the length of the domains. Therefore, chemical pattern dimensions can be used to further tune the pitch of stabilized hierarchical helical morphology. Meanwhile, the formed hierarchical helical structure has a certain range of adaptability to pattern dimensions, which is reflected in changes of domain size.

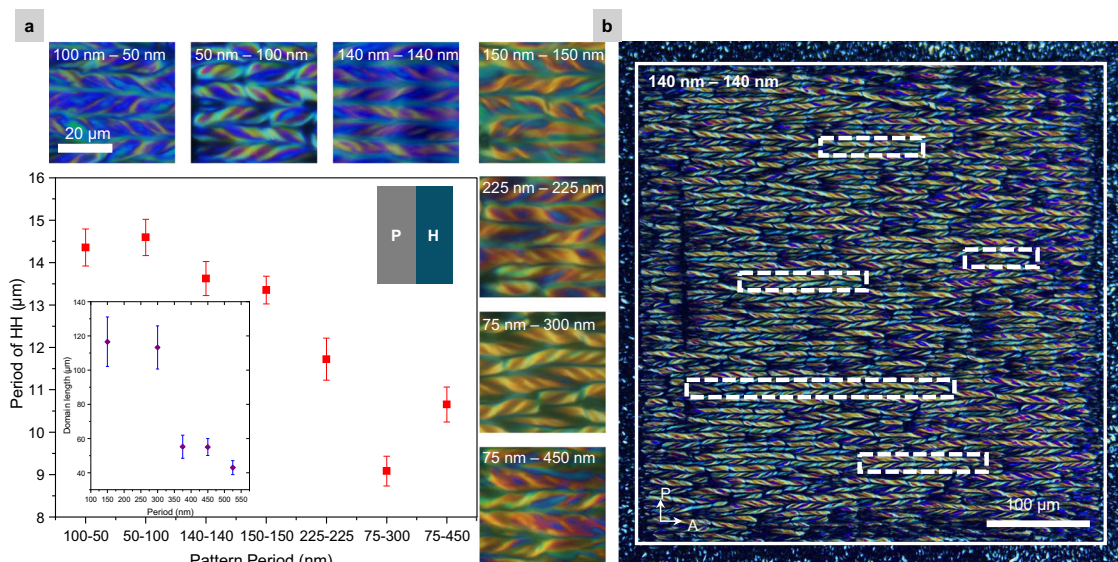


**Fig. 5 | Chemical pattern dimensions impact the hierarchical helical morphology.** **a** Polarized optical micrographs of hierarchical helical morphologies confined on chemical patterns of varying dimensions; Scale bar: 20  $\mu\text{m}$ . The plot shows the periodicity of the morphology as a function of the chemical pattern period. Inset: domain length of the hierarchical helical structures as a function of

pattern period. Data are presented as mean values  $\pm$  SEM, where SEM (standard error of the mean) was calculated as the standard deviation divided by the square root of  $n$ , with  $n=15$ . **b** hierarchical helical morphology confined on the chemical pattern of an area 440  $\mu\text{m} \times 440 \mu\text{m}$ , highlighted domains of morphology; Scale bar: 100  $\mu\text{m}$ .

### Cell thickness affects the volume of 3D helix structure

In addition to chiral dopant concentration and temperature, the pitch of the cholesteric phase can also be modulated by the confinement space. Figure 6a shows the POM images of the morphology as the space between substrates is varied. The film thickness was gradually increased from 100 nm to 12  $\mu\text{m}$ , while keeping other sample characteristics, such as pattern dimension ( $P-W_H$ : 150–75 nm) and PMMAZO concentration (0.05 wt%), constant. Without spacers, the film thickness was around  $94 \pm 30 \text{ nm}$ <sup>43</sup>, and the helix structure just before the phase transition at 40  $^\circ\text{C}$  is shown in Fig. 6a. Optical observations revealed that the structure is similar to the one shown in Fig. 2 at 32.3  $^\circ\text{C}$ , confirming that both confinement and temperature can have a similar effects on morphology. The average periodicity of the helix at this point was smallest, measured at 5.86  $\mu\text{m}$ . Increasing the confinement depth to 1.5  $\mu\text{m}$  resulted in a hierarchical helix with a periodicity of 11.00  $\mu\text{m}$ . For a thickness of 3.5  $\mu\text{m}$ , using the same conditions applied to Fig. 1d, the periodicity of helix was measured at 12  $\mu\text{m}$ . Further increasing the confined thickness to 6  $\mu\text{m}$ , resulted in a period of 15.15  $\mu\text{m}$ , and a 12  $\mu\text{m}$  thickness produced the largest morphological period of 20.54  $\mu\text{m}$ . The periodicity of the hierarchical helix at each film thickness is plotted in Supplementary Fig. 7. This increment in the period due to thickness variation was found to be insensitive to smaller fluctuations in film thickness. A significant shift in periodicity was only observed when the thickness was raised from 100 nm to 1.5  $\mu\text{m}$ . It is also important to note the morphological sensitivity to disruptions in the chemical pattern or the polymer brush. For cell thicknesses of 6  $\mu\text{m}$  and above, numerous regions of structural distortion were observed, along with failure to generate helical morphology over large domain sizes. The PMMAZO brush has demonstrated the ability to control the LC molecular orientation over several micrometers<sup>44</sup>. The anchoring energies from both the top and bottom substrates facilitate the formation of hierarchical helical structure of more than tens of micrometers. As cell thickness increases, the formed helix becomes larger in size to adapt to the wider space. However, the favorable anchoring condition from the chemical pattern on the bottom substrate and the PMMAZO-anchored top substrate weakens, disrupting the favorable environment. This weakened interaction leads to defects and distortions in the stable morphology.

Using simulations, we compare the helical structure confined in domains of 100 nm and 200 nm height (Supplementary Fig. 8) to examine the effect of domain height on the size of the helical structures. According to the total free energy plot (Fig. 6b), computed as the integral of the sum of elastic and thermotropic energy contributions, the energy curve flattens over time. This flattening indicates that the system is approaching a stable or metastable state at the point of helical structure formation. The resulting director field for both confinement heights is shown in Fig. 6c (left). Here, we plot the average director vectors at each node in the spatial mesh. Colors represent their alignment with the  $z$ -axis, effectively visualizing the long-range orientational twist. The 3D cells (Fig. 6c right) illustrate the director field across  $YZ$  plane imposed on the disclination lines formed in each domain. We observe that the taller domain (200 nm) results in a larger helical structure, while the shorter domain (100 nm) produces a more compact helix with a smaller period. This suggests that the height of the domain or the size of 3D space directly influences the helical periodicity, with reduced confinement leading to an increase in the helical structure size.

### Nano-mechanics of LC thin film with hierarchical helix structure

Until now, most research on the cholesteric phase of liquid crystals has focused on optical properties<sup>45–47</sup>, including studies on pitch attenuation<sup>48</sup>, twisting sense inversion<sup>49</sup>, or film coupling of both handed structures<sup>50</sup>. Additionally, some studies have employed cholesteric films as optical sensors<sup>51</sup>, since stress modulation can alter the pitch of the Chol. phase<sup>51,52</sup>, thereby tuning the reflective color of the film according to the stress level. In this study, we go beyond the modulation of reflected colors induced by pitch attenuation through various methods. Given the hierarchical nature of the morphology assembled on the patterned region and its similarity to the Bouligand structure, it's necessary to explore other properties conferred by this structure. Therefore, a soft template containing a hierarchical helix structure was fabricated using the solution of compounds listed in Supplementary Fig. 9. The chemical pattern dimensions were adjusted to match the pitch of the cholesteric phase as follows:  $P=170 \text{ nm}$ ;  $W_P$  &  $W_H=85 \text{ nm}$ <sup>38</sup>. At the transition point between the Chol. phase and BPI, when the HH structure is most prominent, UV irradiation was

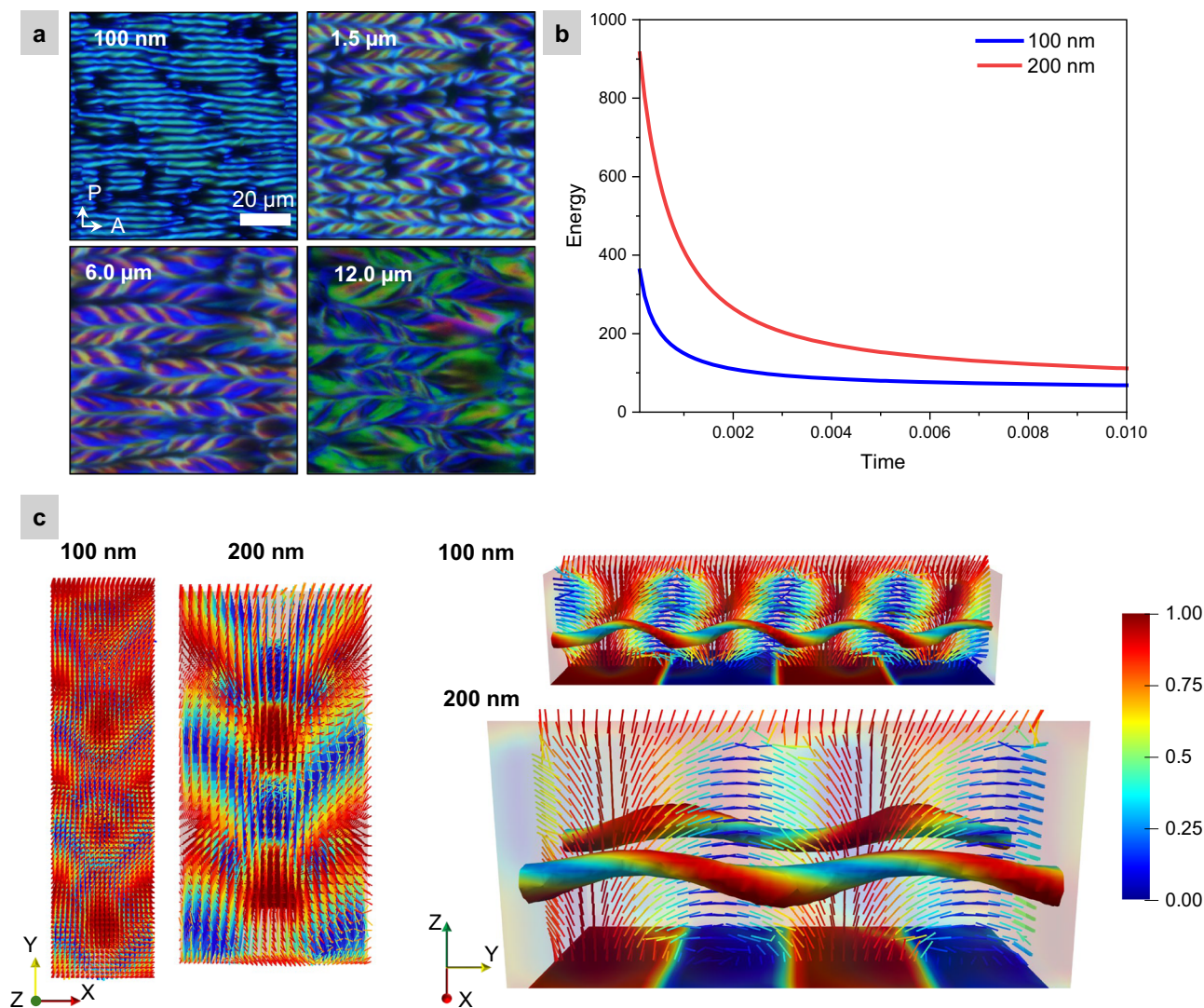


**Fig. 6 | Hierarchical helical morphology confined in different film thickness.** **a** Cholesteric phase confined in films with thicknesses of 100 nm, 1.5  $\mu\text{m}$ , 6  $\mu\text{m}$ , and 12  $\mu\text{m}$ . Scale bar: 20  $\mu\text{m}$ . **b** Energy vs. time plot for simulated helical structure in different domain heights. **c** Simulated helical structures confined within domain heights of 100 nm and 200 nm, shown as top-down views (left) and corresponding

3D cells (right) illustrating disclination lines and director field distribution across the YZ plane. Here we represent the orientation of the molecules as segments which are colored according to their alignment with respect to the z-axis, where value 0 (blue) represents orthogonal alignment and value 1 (red) parallel alignment.

employed to polymerize the structure. To investigate the structure-property relationship, both PeakForce quantitative nano mechanics (QNM) and nano-dynamic mechanical analysis (nDMA) of the structure were performed using a Bruker AFM. PeakForce tapping technology can be used to map the modulus with nanometer-scale resolution in topography. Furthermore, in nDMA, as shown in Fig. 7a, the AFM probe indents the surface of the sample while it is oscillated at various frequencies<sup>53</sup>. The response of the material is then measured in terms of both amplitude and phase shift of the oscillation. The response is calibrated using a reference sapphire sample to calculate the dynamic mechanical properties of the sample, including storage modulus, loss modulus, and loss tangent. These properties are essential for understanding viscoelastic behavior which reflects the ability of a material to dissipate energy or recover after deformation.

The optical and AFM height sensor images of the randomly oriented Chol. phase outside the pattern area and the pattern-directed hierarchical helical structure are shown in Fig. 7b–d respectively. The DMT modulus of both structures in Fig. 7e demonstrates that both are stiff materials, with the highest Young's modulus measured at 8 GPa, showing relatively no major difference between them. The calculated

and averaged dynamic mechanical properties of samples are plotted as function of frequency applied and shown in Fig. 7f–h. The stabilized morphology is labeled as the HH structure, and the randomly oriented structure outside the pattern is labeled as CLCs. Dynamic mechanical properties were tested at five different locations, both within and outside the patterned region, across varying frequencies. The results for each individual test are provided in the Supplementary Fig. 10, 11. The storage modulus  $E'$  data, a measure of the structure's ability to store elastic energy, shows a linear increase in  $E'$  with increasing frequency for both morphologies (Fig. 7f). However, the hierarchical 3D structure exhibited around 25% increase in storage modulus compared to the randomly oriented CLCs, likely due to its unidirectional morphology and 3D structure enhancing elasticity. In contrast, the loss modulus  $E''$ , which indicates the ability to dissipate stress via heat, showed a 5% difference between the two structures at lower frequencies (Fig. 7g). Only at higher frequencies did the HH morphology demonstrate a 20% increment. Whereas the loss tangent value, which is less than one, denotes the ability of both structures to behave elastically and store more energy than they dissipate. The response from both the HH and CLCs first increased with increasing frequency and

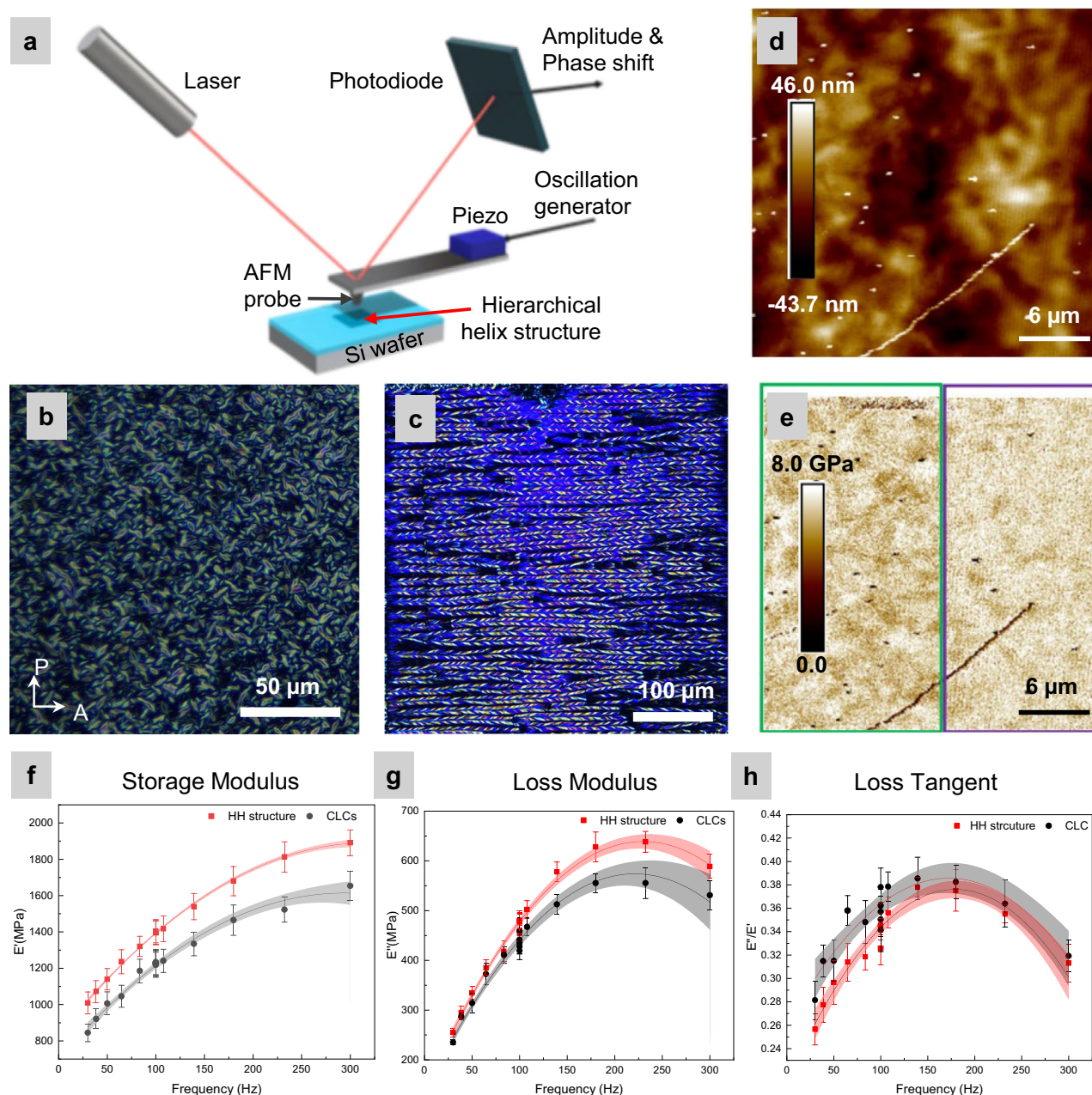


**Fig. 7 | Nano-mechanics of soft-templated hierarchical helical morphology.**

**a** Schematic of the atomic force microscopy (AFM) setup used for nanoscale dynamic mechanical analysis (nDMA). Polarized optical microscopy images of the **(b)** soft-templated randomly oriented cholesteric phase CLCs and **(c)** hierarchical helical morphology (HH). **d** AFM height sensor images of the CLCs and hierarchical

helical structure (HH). **e** Static Modulus of the film for CLCs and HH structure calculated using the DMT method. **f–h** Mechanical properties of CLCs and HH structure calculated from nDMA examination. **f** Storage modulus, **g** loss modulus, **h** loss tangent. Data are presented as mean  $\pm$  SEM,  $n = 5$  independent measurements.

then diminished at higher frequencies (Fig. 7h). Additionally, the higher recovery and dissipation in CLCs compared to the HH morphology can be attributed to the different CLC alignments, which act as disclination lines that effectively dissipate impact forces.

#### Uniaxial deformation of the polymerized hierarchical helical structure

To assess the mechanical robustness of the hierarchical structure, 6 μm thin free-standing films were subjected to uniaxial stretching. To assist the tensile testing of such freestanding membranes and to adapt the samples to a manual tensile machine mounted under an optical microscopy, they were embedded in a flexible polydimethylsiloxane PDMS enclosure to provide mechanical support and

ensure effective stress transfer during testing. PDMS is widely used as a supporting matrix in mechanical deformation studies due to its ability to preserve film integrity and enable reproducible strain application. In this system, the morphology was confined within chemically patterned regions of varying widths (100 μm, 120 μm, 140 μm, and 160 μm) and a fixed length of 440 μm. Strain along the helical axis was calculated as a percentage using the relation:

$$\varepsilon = \frac{L - L^0}{L^0}, \quad (1)$$

where  $L_0$  is the initial width of the patterned region and  $L$  is the width after stretching in the x direction.

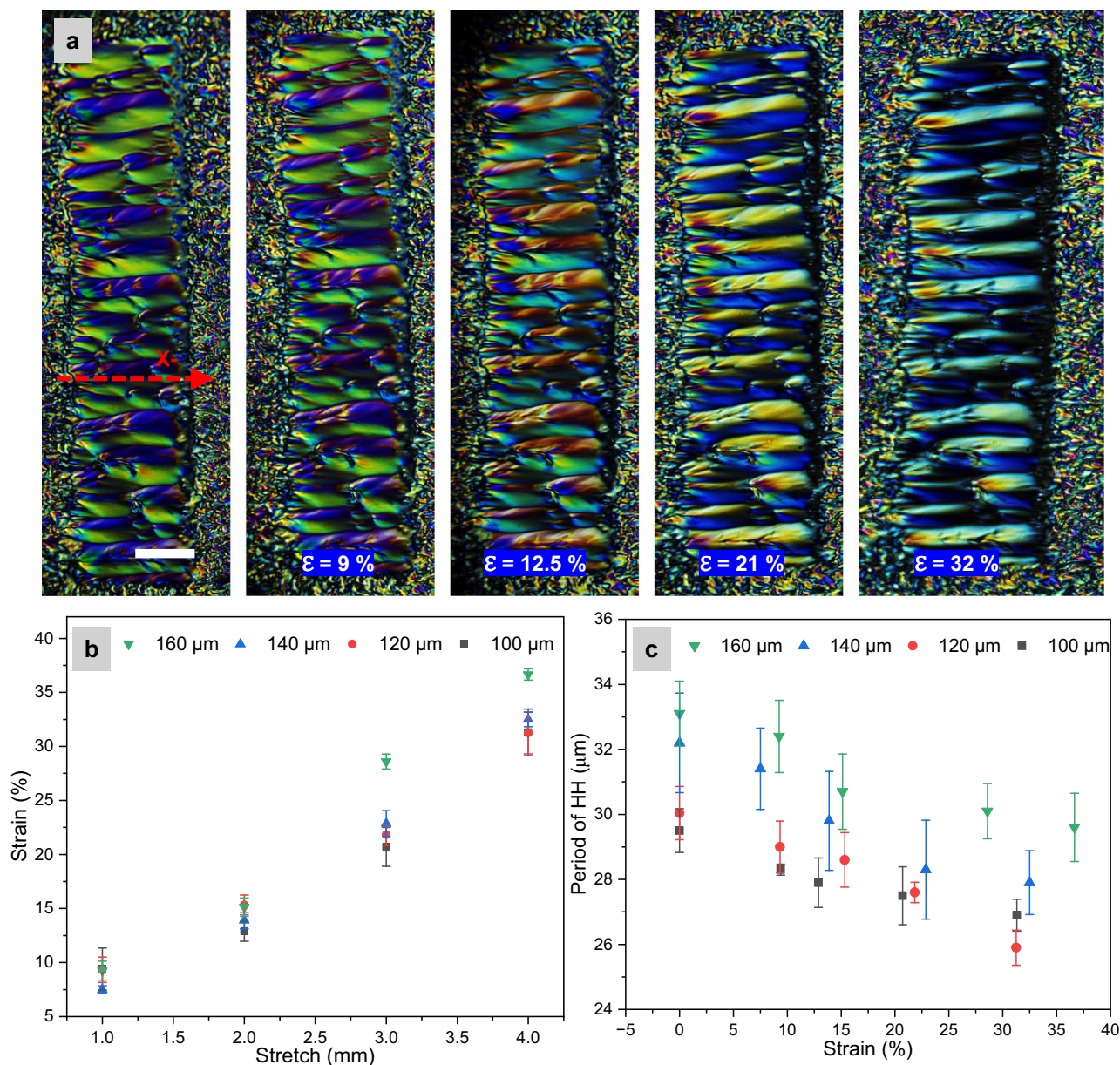


**Fig. 8 | Elastic reversible deformation of hierarchical helical morphology under uniaxial stretch. a** POM images of HH morphology confined to 100  $\mu\text{m}$ -wide patterned regions and stretched along the  $X$ -direction shown using red arrow; Scale

bar: 50  $\mu\text{m}$ . **b** Plot of calculated strain (%) versus stretch distance for different pattern widths. **c** Periodicity of the HH morphology as a function of applied strain (%) across varying pattern widths. Data represent mean  $\pm$  SEM;  $n = 15$ .

Initially, under transmission mode optical microscopy, the rope like morphology exhibited well defined birefringent domains corresponding to oppositely twisted helices. The sample was stretched uniaxially along the  $X$ -direction from 1 mm to 4 mm using a manual tensile machine shown in Supplementary Fig. 12. Representative POM images for the 100  $\mu\text{m}$  wide pattern are shown in Fig. 8a, with additional data for 120 to 160  $\mu\text{m}$  wide regions provided in Supplementary Fig. 13. To quantify mechanical deformation, the width of each patterned region was measured at every stretch increment. Corresponding strain percentages, presented in Fig. 8b, indicate a uniform mechanical response for 100 to 140  $\mu\text{m}$  patterns, with strain increasing from -9% at 1 mm to around 32% at 4 mm. In contrast, the 160  $\mu\text{m}$  wide pattern exhibited a nonlinear response, reaching a strain of 28.5% at 3 mm and peaking at 36% at 4 mm stretch. Figure 8c presents the normalized periodicity of the hierarchical morphology as a function of strain percentage. All patterns exhibited a monotonic decrease in periodicity for increasing strain %, confirming compression of the

cholesteric pitch under uniaxial strain. For instance, the 100  $\mu\text{m}$  pattern showed a drop in periodicity from 29.5  $\mu\text{m}$  to 26.9  $\mu\text{m}$ , while the 160  $\mu\text{m}$  pattern decreased from 33.1  $\mu\text{m}$  to 29.6  $\mu\text{m}$ . Narrower patterns (100 and 120  $\mu\text{m}$ ) exhibited a steeper decline compared to wider ones, suggesting enhanced pitch compressibility or greater mechanical constraint in narrower regions. These structural changes were accompanied by distinct color shifts from magenta to yellow and green to blue, indicating a nanoscale modulation of the cholesteric pitch, consistent with a blue shift in reflected wavelengths under strain. This behavior aligns with prior reports where elastic deformation induces optical tunability via pitch compression<sup>54</sup>. Beyond 4 mm stretch, the film fractured mechanically, though the hierarchical helical morphology remained intact. Upon release, the morphology recovered its original color and periodicity, demonstrating reversible deformation. The morphology was also examined under uniaxial stretching along the  $y$ -direction using optical microscopy, as shown in Supplementary Fig. 14. At a 3 mm stretch, the patterned region

extended to 526.89  $\mu\text{m}$ , corresponding to a calculated strain of 18.96%. The resulting optical changes were noticeably less vibrant compared to stretching along the  $x$ -direction, suggesting anisotropic optical response. To further evaluate strain response, a 12  $\mu\text{m}$  thick film was tested under uniaxial tensile loading along both  $x$ - and  $y$ -directions. The optical images and corresponding analytical data are presented in Supplementary Figs. 15, 16. Consistent with the 6  $\mu\text{m}$  film, stretching along the  $x$ -direction in the 12  $\mu\text{m}$  sample also induced a clear blue shift, and the original dimensions and vivid birefringent texture were recovered upon strain release, confirming reversible deformation (Supplementary Fig. 15). In contrast, for  $y$ -direction stretching, the 12  $\mu\text{m}$  film withstood strain up to 22.38% before mechanical failure (Supplementary Fig. 16). These results demonstrate that the hierarchical helical structure exhibits reversible deformation and tunable optical response under uniaxial strain, with enhanced pitch compressibility in narrower patterns. The films show clear anisotropic behavior, with greater optical modulation and mechanical robustness along the  $x$ -direction compared to the  $y$ -direction.

### Evaluating electro optic sensitivity of the polymerized hierarchical helical structure

The electro optic response of the hierarchical helical morphology was evaluated by applying a constant direct current voltage across a sandwiched LC cell. A 3.5  $\mu\text{m}$  thick LC cell containing pure cholesteric solution without reactive monomers was used to study the electric field response of the hierarchical helix. A constant DC voltage of 5 V was applied and held steady while the optical response of the sample was recorded over time, as shown in Fig. 9a. Initially, the patterned region did not exhibit any hierarchical morphology. Around 30 s after the application of voltage, the morphology began to emerge across the patterned area, and by 55 s, it was fully developed. Between 40 and 130 s, a progressive color shift was observed, indicating a blue shift in reflected wavelength consistent with pitch compression under the applied electric field. At -140 s, the morphology underwent a phase transition into the blue phase. The overall evolution closely mirrors the thermally induced response of the same structure. A movie of the full optical evolution under applied voltage is provided in the Supplementary Movie 1. Upon removal of the electric field, the morphology transitioned back into the cholesteric phase. Within a few seconds, the hierarchical morphology reappeared across the patterned area. A reverse color shift was observed, progressing from yellow to magenta and eventually dark, indicating a red shift associated with pitch relaxation. At 11 s, the morphology appeared prominently in magenta, followed by a gradual loss of contrast. By 50 s, the patterned region appeared blank, with no visible traces of the hierarchical helices, suggesting full relaxation and unwinding of the structure. Subsequently, a partially polymerized film was tested under electric field to evaluate its retained electro-optic functionality. In this case, a higher DC voltage of 9.1 V was required to induce a response. Similar to the pure cholesteric solution, the morphology exhibited a clear blue shift, with the color gradually transitioning from green to dark blue as shown in Fig. 9b. The optical response progressed uniformly across the patterned area, indicating effective field penetration and consistent pitch modulation throughout the morphology. Notably, the stripe-like hierarchical features remained intact during the color change, confirming structural stability under the applied field.

### Discussion

By tuning the chemically patterned substrate to match the pitch of the cholesteric phase, a metastable microstructure exhibiting both left- and right-handed twists is stabilized. These results highlight the intricate interplay between the periodic anchoring provided by the chemical pattern and the chiral nanoscale organization of the cholesteric liquid crystal. Notably, the rope-like texture observed under the optical microscope closely resembles the texture typically associated with

the twist-bend nematic (Ntb) phase of LCs<sup>55,56</sup>. In the Ntb phase, the interplay between twist and bend deformations of bent-core molecules produces a heliconical arrangement, where the local director tilts obliquely with respect to the helical axis. V. Borshch et al.<sup>57</sup> have linked the structural organization of the Ntb phase to the Bouligand arches proposed by Bouligand et al.<sup>58</sup>, with a periodicity in the range of 0.8 – 8 nm<sup>57</sup>. However, unlike chiral phases that display either a left- or right-handed helicoidal structure, the achiral nature of the Ntb phase allows for the coexistence of domains with both twisting senses. In this study, beyond the left-handed chirality imparted by the chiral dopant S-811, the interaction between the surface pattern and the intrinsic chirality of the doped LC phase provides insight into the role of substrate-induced anchoring in controlling chiral organization. Furthermore, the formation of a microscale helix from a cholesteric phase with a nanometer scale pitch is a notable phenomenon. Even under extreme confinement of 100 nm, the morphological period measures ~5.86  $\mu\text{m}$  and increases linearly with confinement. A similar trend is observed in the Ntb phase, where the morphology period correlates directly with the confinement space via the Helfrich–Hurault mechanism<sup>55</sup>. The coexistence of microscale helix formation with both left- and right-handed twists defines a distinct morphological state. Interestingly, the hierarchical helical (HH) morphology observed in our system exhibits clear parallels with previously reported modulated cholesteric textures that feature curved domain boundaries and focal-point reflections, reminiscent of focal conic domains in smectic phases<sup>59</sup>. On length scales much larger than the cholesteric pitch, cholesterics can display smectic-like behavior due to their layered helicoidal structure, allowing analogies to smectic focal conics and confocal domains to emerge. Similar to these 2D modulated textures, the HH morphology shows curved and periodically modulated director fields, as confirmed by both simulations and confocal microscopy. The lateral shift of the helical axis, coupled with vertical modulation across the film thickness, produces oblique, rope-like helices and nested periodic domains. A key distinction, however, lies in the dimensionality: while previously reported cholesteric textures were confined to planar (2D) modulations, the HH morphology extends these principles into a three-dimensional regime. The observed half-pitch phase shifts across opposite surfaces, evident in both experiments and simulations, are reminiscent of Bouligand's description of confocal cholesteric domains<sup>60</sup>, but in our case, such phase modulation propagates throughout the film thickness, resulting in a fully 3D hierarchical structure. Thus, the HH morphology can be understood as a three-dimensional generalization of confocal-like cholesteric ordering, arising from the combined effects of intrinsic twist, patterned surface anchoring, and elastic frustration.

Relying on computational simulation, the model describing cholesteric LC phase has been set up first as a Bouligand-like structure of helical twist cylinders. To input the Bouligand structure, we initialize the simulation by giving the directors a long-range twist with the helical axis perpendicular to the patterned boundary conditions. Then, by dividing the domain into two halves (top half and bottom half), we rotate the helix layers 45-degrees in either direction to create a Bouligand-like structure where the helices are treated as individual fibers, and the Bouligand twisting axis is the vertical. The effect is that two layers of orthogonal helical arrays meet, and as the system moves to a configuration of lower energy, it results in a large, well-defined helical twisting structure, shown using an iso-surface of the degree of orientation metric  $|\mathbf{Q}|^2$ . This indicates a region of low orientational order inside the helical structure, located at the point of contact between the two Bouligand layers, and higher order outside, where we find just a cholesteric twisting director field. These areas away from the helix evolve to achieve high degrees of orientation, and the iso-surface at the helix is isolated once the system reaches a relatively stable or metastable configuration, indicated by the flattened energy curve in Fig. 6b. Additionally, the patterned color indicates that the director is

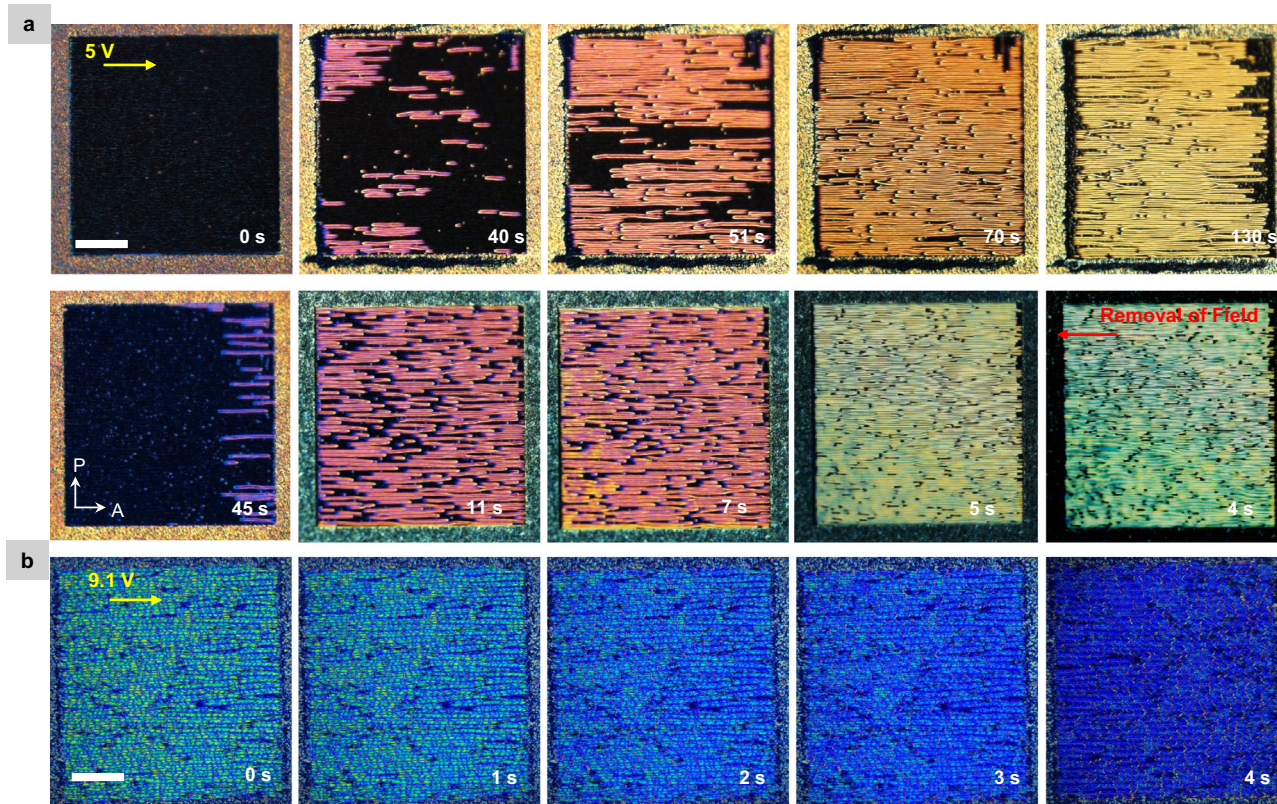


**Fig. 9 | Electro-optic response of hierarchical helical (HH) morphology.** **a** Time-lapse POM images of morphology under constant DC voltage of 5 V (top row: left to right) and after removal of the field (bottom row: right to left). **b** Partially polymerized morphology under a DC field of 9.1 V at different time intervals. Scalebar: 100  $\mu\text{m}$ .

twisting around the helix. To obtain opposite twist helices, we assume that the Bouligand-like structures come in pairs, with one side having a clockwise twist in the  $z$ -direction and the other a counter-clockwise twist. With this consideration, the paired helices are mirrored images of each other, with opposite helical twist as seen in Fig. 2. It should be noted that simulation testing shows that the periodic boundary conditions imposed on the sides is necessary to stabilize the helical twisting structures since otherwise, they will eventually drift apart and escape through Neumann boundary conditions. This agrees with the experimental results since we observe that several repeated columns of helical structures are stabilized over the pattern region. So, by imposing periodic boundary conditions on the sides parallel to the helical axis we are effectively simulating a column array of alternate twist helical structures which is like experiments. While the simulation was initialized using a Bouligand-inspired arrangement of oppositely twisted helices, our system is not a direct replica of biological Bouligand structures. Instead, it functions as a soft matter analogue: the hierarchical helical morphology arises from the interplay of confinement, patterned anchoring, and elastic frustration in cholesteric liquid crystals. The resulting three dimensionally modulated helicoidal structure exhibits periodic layering and lateral curvature, reminiscent of Bouligand architecture. Notably, the disclination lines observed in the simulations are a natural result of the intrinsic cholesteric twist and surface constraints, and they form an essential part of the self-organized, hierarchical structure. To test the linear relationship between domain height and helical size, we perform a similar simulation in a domain twice as tall and wide, with equal length in the helical direction. All of the model parameters, including the twist parameter  $q_0$ , elastic, and thermotropic parameters, are the same in both scenarios. However, the initial condition is scaled to fit the new domain size. In Fig. 6, we can compare the helix sizes by noticing that the alternating red-blue pattern is about twice as large, both in period and size, when

compared with the smaller domain, which agrees with experiments. When viewed from above (Supplementary Fig. 8), we can see that the plot of the directors presents a chevron pattern, which is similar to experimental results. In the simulation, we found that increasing the domain size does lead to larger helices, but there is a limit. At some point, the helical structures form over such long distances that they can no longer be stabilized by the model. This is likely due to the coherence length, which is used to nondimensionalize the model parameters and gives a characteristic length for which the forces in the material interact to form defects. Therefore, comparing domains of height 100 nm to 1500 nm would likely require a different set of parameters. However, our results do show a positive correlation between domain height and helical size.

The resulting cholesteric hierarchical helical structure provides a framework for understanding the self-assembly mechanism of chiral liquid crystals on chemically patterned surfaces, but also offers a means to address their inherent weak mechanical properties of soft materials by mimicking the Bouligand structure in nature. Especially in the thin film regime, achieving enhanced mechanical properties while retaining optical tunability is critical for next-generation materials, particularly in wearable devices or artificial skin. Soft materials with optimized mechanical performance could surpass traditional semiconductor materials, offering enhanced durability and adaptability in flexible electronics. In this study, we introduce a system that employs a directed self-assembly approach to harness the properties of a highly chiral cholesteric phase, resulting in a structure that integrates photonic and mechanical functionalities. A key feature of the components used to template the hierarchical helical structure is that they exhibit chromogenic effects as a photonic shape memory polymer in the blue phase liquid crystal temperature range<sup>61</sup>. The fabricated blue phase structure enables shape memory programming by locally deforming the blue phase network and storing the temporary shape until

temperature recovery. However, when the temperature shifts to the cholesteric phase, the molecules reassemble into a hierarchical helix structure only in the presence of a chemically patterned surface. More importantly, the structural thin film exhibits a distinct mechanical response. The mechanical behavior of Bouligand structures has been extensively studied in both natural and synthetic systems, with a focus on bulk samples. In biological Bouligand architectures, elastic modulus values range from 0.1–25 GPa, with the highest value ~70 GPa found in the impact region of the dactyl club of a stomatopod<sup>19,20,23,27</sup>. In contrast, biomimetic Bouligand structures based on CNC composites typically demonstrate Young's modulus values between 0.1–15 GPa<sup>62</sup>, decreasing with increasing strain rates under tensile loading. However, integrated mechanical and optical performance in CNC-composite systems remains rare. Recent studies on hydrogel-PVA systems reported modulus values of ~200 to 450 MPa, combining mechanical strength with optical performance<sup>28</sup>. CNC-based systems often feature a cholesteric fingerprint morphology with a half-pitch value of ~250 nm or more. In comparison, the material in this study achieves a smaller and consistent half-pitch value of ~145 nm for both its cholesteric liquid crystal (CLC), and hierarchical morphology. The half-pitch value was measured based on the chiral dopant's concentration in solution and confirmed by SEM cross-sectional imaging (Supplementary Fig. 17). The nanoscale pitch, coupled with the formation of a microscale hierarchical morphology, notably enhances the mechanical response, leading to observable improvements. Unlike conventional mechanical testing of bulk materials, nanoscale dynamic mechanical analysis (nDMA) was applied to CLC thin films to measure their mechanical response under compressive forces at the nanoscale. The hierarchical morphology, without any additives, demonstrated a 25% increase in elastic modulus and 5 to 20% improvement in viscous modulus compared to the conventional cholesteric structure. The system primarily stored energy in an elastical manner, rather than dissipating it, a response property of its material composition rather than its morphology alone. Another characteristic feature is the precise control over morphological stability at targeted locations through chemical patterning. This approach further enables tuning of functionality, allowing the fine-tuning of mechanical and optical properties with micrometer-scale precision, a level of control not easily achievable in bulk materials. The ability to engineer structural robustness while maintaining optical tunability indicates applicability for flexible photonic devices, responsive coatings, and adaptive optical materials.

We have successfully utilized the cholesteric phase with nanoscale pitch to guide the formation of a microscale hierarchical helix structure on a chemically nanopatterned substrate. The half-pitch of CLCs and the period of chemical pattern was matched to align the helical axis of uniform lying down helices and stabilize the morphology. It was found that the weak homeotropic anchoring from the PMMAZO brush modified top substrate enabled formation of hierarchical helical morphology analogous to the Bouligand structure. Deviating the period of the chemical pattern from the natural pitch of the cholesteric phase (~290 nm) to 525 nm degenerated the helical period to ~9 μm and domain length to ~50 μm. The 3D confinement space affected the morphology characteristics in a similar way thermal treatment and phase transition did. Simulations revealed the structural evolution from initial Bouligand-like configuration to alternating opposite twist helices over time, with lateral and vertical director shifts. These features were experimentally confirmed by confocal fluorescence microscopy across the film thickness, validating the three-dimensional morphology. Under uniaxial tensile loading, a continuous blue shift in reflected color was observed as strain increased up to ~36%, indicating strain-induced pitch compression. Electric field application also resulted in reversible blue shift in both polymerized and non-polymerized films, although the partially polymerized films required higher driving voltage to elicit a comparable optical response. The structure-property correlation examined by nanoscale dynamic

mechanical analysis further reinforced the theory that hierarchical organization improves the robustness. This study provides a basis for further development in soft functional material as wearable devices and sensors, where performance, durability, and adaptability are crucial.

## Methods

### Materials

MLC 2142 and S-811 were purchased from Merck. RM257, RM106, HTG135200-100, HCM006 and Irg651 were obtained from Grand-ichem. Fisher Finest Premium Grade glass slides and coverslips were obtained from Fisher Scientific. Red Nile Dye, Octadecyltrichlorosilane (OTS), heptane, dichloromethane (DCM), chlorobenzene, isopropyl alcohol, and NMP were purchased from MilliporeSigma and used without further purification. The LC polymer brush PMMAZO, poly (6-(4-methoxy-azobenzene-4'-oxy) hexyl methacrylate), was synthesized through a process reported by Stewart and Imrie<sup>63</sup>. 4-hydroxy-4'-methoxyazobenzene was prepared by diazotization of p-anisidine and coupling with phenol. This intermediate was reacted with 1,6-dibromohexane in acetone with potassium carbonate to form 1-bromo-6-(4-methoxy-azobenzene-4'-oxy)hexane. The bromide was then coupled with methacrylic acid, via the potassium methacrylate salt in DMF at 100 °C for 24 h with hydroquinone inhibitor, to yield MMAZO. Polymerization of MMAZO was carried out using nitroxide-mediated controlled radical polymerization (NMP). In a typical reaction, MMAZO (2.3160 g, 6 mmol) was mixed with the NMP initiator (0.0244 g, 0.075 mmol) and the solution was degassed by three freeze-thaw cycles. The mixture was then heated at 120 °C for 24 h under nitrogen. The crude polymer was dissolved in THF and precipitated into petroleum ether. The final polymer had an average molecular weight of  $\sim 1.1 \times 10^5$  g/mol.

**Surface Modification.** A PMMAZO film was deposited on a piranha-cleaned silicon substrate by spin-coating a 0.05 wt% chlorobenzene solution at 4000 rpm for 60 s and annealed at 250.0 °C for 5 min in a nitrogen atmosphere. The non-grafted PMMAZO was removed by sonication in chlorobenzene three times for 5 min, with the 3–4 nm PMMAZO brush remaining. A 40 nm-thick PMMA\_A2 photoresist film was spin-coated onto the PMMAZO brush and baked at 180.0 °C for 5 min. Patterns with an array of stripes were exposed on the resists *via* electron beam lithography with the JEOL 8100FS electron-beam writer at the Center for Nanoscale Materials, Argonne National Laboratory. The exposed substrates were developed in IPA: MIBK for 60 s followed by rinsing with isopropyl alcohol. The oxygen plasma etching transferred the resist pattern onto the PMMAZO brush layer. The PMMA-A2 photoresist was further stripped by NMP through sonication.

**Cell construction.** The glass microscope slides were boiled in a piranha solution (7:3 (v/v) of 98% H<sub>2</sub>SO<sub>4</sub>/30% H<sub>2</sub>O<sub>2</sub>) at 130.0 °C for 1 hr to remove any stains on the surface, followed by washing with DI water and drying with nitrogen. The PMMAZO modified glass and a cleaned Si substrate or a Si substrate with the PMMAZO chemical pattern were placed face-to-face, with a mylar spacer of different thickness, to create a cell with a directed self-assembly approach. The optical cell and the LC were heated above the clearing point and the mixture was injected through capillary action. The system was then slowly cooled to room temperature. The UV irradiation of samples with 21.2 mW cm<sup>-2</sup> (measured at 365 nm) was carried out using an ultraviolet light source (Hamamatsu E11923).

**PDMS membrane enclosure preparation.** Flexible PDMS membranes were prepared by spin-coating a prepolymer mixture of Sylgard 184 (base:crosslinker = 10:1 w/w) at 1000 rpm for 15 s onto a clean glass slide to obtain a film ~100 μm thick. The coated substrate was degassed under vacuum to remove air bubbles and subsequently cured at 95 °C

for 30 min. This thickness provided sufficient flexibility while ensuring mechanical integrity during handling and deformation. To facilitate film transfer, a thin layer of uncured PDMS was spin-coated (1000 rpm) on top of the cured membrane. The polymerized liquid crystal film was gently placed onto the uncured PDMS surface. The assembly was then degassed and cured at 95 °C for 15 min to bond the liquid crystal film to the PDMS membrane. After partial curing, another layer of PDMS was coated on the film and cured at 95 °C for 1 h. The membrane was cut to size and carefully peeled from the silicon substrate for mechanical testing.

**Characterization.** The thickness of the PMMAZO brush was measured by a Woollam VUV-VASE32 variable angle spectroscopic ellipsometer. The JEOL 8100FS electron-beam writer at the Center for Nanoscale Materials, Argonne National Laboratory was used to write chemical patterns. The optical images of the LC cell were obtained with a BX 60 Olympus polarized light microscope. UV-visible spectra were recorded using a spectrophotometer (Flame UV-VIS Ocean Insight). Confocal fluorescence imaging was performed using a Zeiss LSM710 laser scanning microscope in transmission mode equipped with Airyscan 1 for enhanced resolution and signal-to-noise characterization. AFM from Bruker was used for carrying out the nDMA measurements. Gamry potentiostat reference 600 + was used for electric field application across sandwiched LC cells.

**AFM nDMA measurements.** AFM mechanical mapping was conducted on the film surface with the PeakForce Quantitative Nanomechanical Mapping mode of Bruker’s Dimension Icon AFM (using a 30 nm radius tip RTESPA-525-30, purchased from Bruker, USA). These tips were calibrated on the standard samples (purchased from Bruker, USA) via a multistep procedure. First, the deflection sensitivity was calibrated via standard sapphire sample. Second, the spring constant was calculated utilizing the Sader method. The tip radius was monitored both before and after tests to guarantee that the tip radius remained unchanged throughout the experiments. With a PeakForce-QNM operating frequency of 30 Hz, 38.7 Hz, 50 Hz, 64.6 Hz, 83.5 Hz, 100 Hz, 107.8 Hz, 139.25 Hz, 179.9 Hz, 232.3 Hz, 300 Hz. nDMA amplitude is around 0.5 nm. The indentation force is 1000nN. Indentation depth is around 8 nm. Raw data such as force vs Z-displacement curve of each indent were captured along with spatial maps of modulus, topography, and adhesion.

**Uniaxial tensile test.** To apply uniaxial deformation, the PDMS-supported chiral LC films were mounted on a manual tensile stage (Micro Vice Holder, STJ-0116-A, S.T. Japan Inc.) equipped with dual micrometer screw gauges. The samples were stretched incrementally in a stepwise manner along the desired direction, with displacement controlled via the screw gauges (Supplementary Fig. 12). Optical images were recorded at each displacement increment using transmission mode polarized optical microscopy (POM) to monitor structural and optical changes during deformation.

**Numerical methods.** In this work we use a Landau-de Gennes Q-tensor model which has been extended to include long range twisting effects to represent blue phase and cholesteric liquid crystals<sup>64–66</sup>. In this framework, a traceless second order tensor  $\mathbf{Q}$  is used to describe the local average orientation of the liquid crystal molecules and is commonly written in its eigenframe:

$$\mathbf{Q} = s_1(\mathbf{d}_1 \otimes \mathbf{d}_1) + s_2(\mathbf{d}_2 \otimes \mathbf{d}_2) - \frac{1}{3}(s_1 + s_2)\mathbf{I}, \quad (2)$$

with  $\mathbf{d}_i$  being the orthonormal eigenvectors of  $\mathbf{Q}$ , and  $s_i$  being linear combinations of the eigenvalues  $\lambda_i$ . To visualize the director

orientation, we plot the dominant eigenvector  $\mathbf{d}_1$ , which corresponds to the eigenvector associated with the largest eigenvalue of  $\mathbf{Q}$ . The total free energy of the system is expressed as

$$E_{LdG}(\mathbf{Q}) = \int_{\Omega} \left( \Phi(\mathbf{Q}, \nabla \mathbf{Q}) + \frac{1}{\varepsilon} \Psi(\mathbf{Q}) \right) dx, \quad (3)$$

where  $\varepsilon > 0$  is a dimensionless parameter to balance the contribution of each part of the energy. Here, the elastic energy  $\Phi(\mathbf{Q}, \nabla \mathbf{Q})$  includes the tendency of the molecules to align with each other and the chirality of the molecules as follows<sup>66,67</sup>:

$$\Phi(\mathbf{Q}, \nabla \mathbf{Q}) = \frac{L}{2} \left( |\nabla \mathbf{Q}|^2 + 4q_0 \nabla \mathbf{Q} : (\boldsymbol{\epsilon} \cdot \mathbf{Q}) \right), \quad (4)$$

where  $L$  is the elastic parameter,  $q_0 = 2\pi/p$  with  $p$  denoting the chiral pitch<sup>68</sup>, and  $\boldsymbol{\epsilon}$  the Levi-Civita permutation tensor. The thermotropic contribution to the energy  $\Psi(\mathbf{Q})$  is written as

$$\Psi(\mathbf{Q}) = \frac{A}{2} \text{tr}(\mathbf{Q}^2) + \frac{B}{3} \text{tr}(\mathbf{Q}^3) + \frac{C}{4} \text{tr}(\mathbf{Q}^2)^2, \quad (5)$$

where  $A, B$ , and  $C$  are material parameters, with  $B, C \geq 0$  and  $A$  depending on the temperature.

System dynamics are obtained using an  $L^2$ -gradient flow,

$$\mathbf{Q}_t + \eta \left( \frac{\delta E_{LdG}}{\delta \mathbf{Q}} \right) = 0, \quad (6)$$

with  $\eta > 0$  being a time-scale relaxation parameter. To approximate the solutions to this PDE we employ an extension of a numerical method proposed by ref. 69 which uses a Finite Difference scheme in time, and the Finite Element Method in space, which is solved using the software FreeFEM++<sup>70</sup>. Typical parameters for 5CB liquid crystal are nondimensionalized using a coherence length of  $\xi = 100nm$ <sup>67</sup> which yields  $A = -4.48, B = 55.26, C = 45.09, L = 1.0$ , and  $\eta = 9.59$ . A chiral pitch of  $p = 290nm$  is used to obtain the nondimensionalized twist parameter  $q_0 = 20\pi/29$ . To create the figures of simulation data, we use the Paraview<sup>71</sup> visualization software, and show the iso-surfaces of the value  $|\mathbf{Q}|^2$ , and color the image by using  $S = |\mathbf{d}_1 \cdot [0, 0, 1]|$  to show the alignment of the director with the z-axis. The initial condition to recreate a Bouligand-like structure is given by

$$\mathbf{d}_0 = [\sin(4\pi(1 - \tau(z))x + \tau(z)y), \sin(4\pi(1 - \tau(z))x + \tau(z)y), \cos(4\pi(1 - \tau(z))x + \tau(z)y)], \quad (7)$$

$$\mathbf{Q}_0 = 0.7 \left( \mathbf{d}_0 \otimes \mathbf{d}_0 - \frac{|\mathbf{d}_0|^2}{3} \mathbf{I} \right), \quad (8)$$

where  $\tau(z) = 1.0$  when  $z < \frac{h}{2}$  and  $\tau(z) = 0$  otherwise, and with  $h$  denoting the height of the domain. For the boundary conditions, we impose alternating homeotropic-planar Dirichlet boundary conditions on the bottom boundary, a weak anchoring Dirichlet condition in the top boundary which is imposed as a slightly tilted version of the homeotropic case by a zenith angle of  $\pi/8$  radians given by

$$\mathbf{d}_{top} = \left[ \sin\left(\frac{\pi}{8}\right), 0, \cos\left(\frac{\pi}{8}\right) \right], \quad (9)$$

$$\mathbf{Q}_{top} = \mathbf{d}_{top} \otimes \mathbf{d}_{top} - \frac{1}{3} \mathbf{I}, \quad (10)$$

and periodic boundary conditions are considered on all the lateral sides of the domain.

## Data availability

The data generated in this research work are provided in the main text and Supporting Information. All data are available from the corresponding author upon request.

## Code availability

The code presented in this study was created using FreeFEM ++, and data was visualized with ParaView as described in the Methods section. The code used in this work and instructions for installing and running the software can be obtained from the following repository: <https://github.com/JustinSwain/Cholesteric3D>.

## References

- Iqbal, S. M. A., Mahgoub, I., Du, E., Leavitt, M. A. & Asghar, W. Advances in healthcare wearable devices. *npj Flex. Electron* **5**, 9–14 (2021).
- Mahato, K. et al. Hybrid multimodal wearable sensors for comprehensive health monitoring. *Nat. Electron* **7**, 735–750 (2024).
- Rich, S. I., Wood, R. J. & Majidi, C. Untethered soft robotics. *Nat. Electron* **1**, 102–112 (2018).
- Bang, J. et al. Bioinspired electronics for intelligent soft robots. *Nat. Rev. Electr. Eng.* **1**, 597–613 (2024).
- Choi, S. et al. Highly flexible and efficient fabric-based organic light-emitting devices for clothing-shaped wearable displays. *Sci. Rep.* **7**, 6424–6428 (2017).
- Yin, L. et al. A stretchable epidermal sweat sensing platform with an integrated printed battery and electrochromic display. *Nat. Electron* **5**, 694–705 (2022).
- Lin, M., Hu, H., Zhou, S. & Xu, S. Soft wearable devices for deep-tissue sensing. *Nat. Rev. Mater.* **7**, 850–869 (2022).
- Ates, H. C. et al. End-to-end design of wearable sensors. *Nat. Rev. Mater.* **7**, 887–907 (2022).
- Münzenrieder, N. et al. Stretchable and conformable oxide thin-film electronics. *Adv. Electron. Mater.* **1**, n/a (2015).
- Kim, D. et al. Optimized structural designs for stretchable silicon integrated circuits. *Small* **5**, 2841–2847 (2009).
- Sim, K. et al. Fully rubbery integrated electronics from high effective mobility intrinsically stretchable semiconductors. *Sci. Adv.* **5**, eaav5749 (2019).
- Kim, D. et al. Materials and noncoplanar mesh designs for integrated circuits with linear elastic responses to extreme mechanical deformations. *Proc. Natl Acad. Sci. - PNAS* **105**, 18675–18680 (2008).
- Jang, K. et al. Self-assembled three dimensional network designs for soft electronics. *Nat. Commun.* **8**, 1–15894 (2017).
- Molina-Lopez, F. et al. Inkjet-printed stretchable and low voltage synaptic transistor array. *Nat. Commun.* **10**, 2676–10 (2019).
- Park, M. et al. Highly stretchable electric circuits from a composite material of silver nanoparticles and elastomeric fibres. *Nat. Nanotech* **7**, 803–809 (2012).
- Choi, S. et al. Highly conductive, stretchable and biocompatible Ag–Au core–sheath nanowire composite for wearable and implantable bioelectronics. *Nat. Nanotech* **13**, 1048–1056 (2018).
- Li, Y. et al. Achieving tissue-level softness on stretchable electronics through a generalizable soft interlayer design. *Nat. Commun.* **14**, 4488 (2023).
- Gong, S., Yap, L. W., Zhu, B. & Cheng, W. Multiscale soft–hard interface design for flexible hybrid electronics. *Adv. Mater. (Weinh.)* **32**, e1902278–n/a (2020).
- Weaver, J. C. et al. The stomatopod dactyl club: a formidable damage-tolerant biological hammer. *Science* **336**, 1275–1280 (2012).
- Yang, R., Zaheri, A., Gao, W., Hayashi, C. & Espinosa, H. D. AFM identification of beetle exocuticle: bouligand structure and nanofiber anisotropic elastic properties. *Adv. Funct. Mater.* **27**, np–n/a (2017).
- Sharma, V., Crne, M., Park, J. O. & Srinivasarao, M. Structural origin of circularly polarized iridescence in jeweled beetles. *Science* **325**, 449–451 (2009).
- Lenau, T. & Barfoed, M. Colours and metallic sheen in beetle shells - a biomimetic search for material structuring principles causing light interference. *Adv. Eng. Mater.* **10**, 299–314 (2008).
- Amini, S., Tadayon, M., Idapalapati, S. & Miserez, A. The role of quasi-plasticity in the extreme contact damage tolerance of the stomatopod dactyl club. *Nat. Mater.* **14**, 943–950 (2015).
- Gao, H., Ji, B., Jager, I. L., Arzt, E. & Fratzl, P. Materials become insensitive to flaws at nanoscale: Lessons from nature. *Proc. Natl Acad. Sci.* **100**, 5597–5600 (2003).
- Yin, Z., Hannard, F. & Barthelat, F. Impact-resistant nacre-like transparent materials. *Science* **364**, 1260–1263 (2019).
- Gao, H. et al. Mass production of bulk artificial nacre with excellent mechanical properties. *Nat. Commun.* **8**, 287–288 (2017).
- Zimmermann, E. A. et al. Mechanical adaptability of the Bouligand-type structure in natural dermal armour. *Nat. Commun.* **4**, 2634 (2013).
- Tang, Y., Lu, C. & Xiong, R. Biomimetic mechanically robust chiroptical hydrogel enabled by hierarchical bouligand structure engineering. *ACS nano* **18**, 14629–14639 (2024).
- Cui, P. et al. Bioinspired bouligand-structured cellulose nanocrystals/poly(vinyl alcohol) composite hydrogel for enhanced impact resistance. *ACS Appl. Mater. Interfaces* **16**, 53022–53032 (2024).
- Xiong, R., Wu, W., Lu, C. & Cölfen, H. Bioinspired chiral template guided mineralization for biophotonic structural materials. *Adv. Mater. (Weinh.)* **34**, e2206509–n/a (2022).
- Stoykovich, M. P. et al. Directed self-assembly of block copolymers for nanolithography: fabrication of isolated features and essential integrated circuit geometries. *ACS Nano* **1**, 168–175 (2007).
- Ouk Kim, S. et al. Epitaxial self-assembly of block copolymers on lithographically defined nanopatterned substrates. *Nature* **424**, 411–414 (2003).
- Arora, H. et al. Block copolymer self-assembly-directed single-crystal homo- and heteroepitaxial nanostructures. *Science* **330**, 214–219 (2010).
- Doerk, G. S. et al. Enabling complex nanoscale pattern customization using directed self-assembly. *Nat. Commun.* **5**, 5805 (2014).
- Martínez-González, J. A. et al. Directed self-assembly of liquid crystalline blue-phases into ideal single-crystals. *Nat. Commun.* **8**, 15854 (2017).
- Nakajima, K., Mitsuhashi, S., Cho, S. & Ozaki, M. Slanted structure of blue phase ii self-aligned on one-dimensional patterned surfaces. *ACS Appl. Mater. Interfaces* **15**, 40054–40061 (2023).
- Liu, S., Marinčič, M., Nys, I., Ravnik, M. & Neyts, K. Photopatterned anchoring stabilizing monodomain blue phases. *ACS Appl. Mater. Interfaces* **16**, 68579–68589 (2024).
- Emeršič, T. et al. A generalizable approach to direct the self-assembly of functional blue-phase liquid crystals. *Adv. Funct. Mater.* **32**, n/a (2022).
- Li, X. et al. Engineering the anchoring behavior of nematic liquid crystals on solid surface by varying the density of liquid crystalline polymer brush. *Soft Matter* **14**, 7569–7577 (2018).
- Zhixuan Jia. et al. Engineering the uniform lying helical structure in chiral nematic liquid crystals: from morphology transition to dimension control. *Cryst. (Basel)* **11**, 414 (2021).
- Giovanni Carbone, D. aniel. et al. Uniform lying helix alignment on periodic surface relief structure generated via laser scanning lithography. *Liq. Cryst.* **544**, 37–49 (2011).
- Kyoung-S. P., Ji-H. B., You-J. L., Jae-H. K. & Chang-J. Y. Effects of pretilt angle and anchoring energy on alignment of uniformly lying helix mode. *Liq. Cryst.* **43**, 1184–1189 (2016).

43. Li, X. et al. Directed self-assembly of nematic liquid crystals on chemically patterned surfaces: morphological states and transitions. *Soft matter* **12**, 8595–8605 (2016).
44. Xiao, Li. et al. Engineering the anchoring behavior of nematic liquid crystals on solid surface by varying the density of liquid crystalline polymer brush. *Soft Matter* **14**, 7569–7577 (2018).
45. Liu, J. et al. Visible-light-programmed patterning in dynamically bonded cholesteric liquid crystal elastomer. *Nat. Commun.* **15**, 10367–11 (2024).
46. Kobashi, J., Yoshida, H. & Ozaki, M. Planar optics with patterned chiral liquid crystals. *Nat. Photon* **10**, 389–392 (2016).
47. Mitov, M. & Dessaud, N. Going beyond the reflectance limit of cholesteric liquid crystals. *Nat. Mater.* **5**, 361–364 (2006).
48. Xiang, J. et al. Electrically tunable selective reflection of light from ultraviolet to visible and infrared by heliconical cholesterics. *Adv. Mater.* **27**, 3014–3018 (2015).
49. Eelkema, R. et al. Nanomotor rotates microscale objects. *Nat. (Lond.)* **440**, 163 (2006).
50. Matranga, A. et al. BiomiMetic reflectors fabricated using self-organising, self-aligning liquid crystal polymers. *Adv. Mater. (Weinh.)* **25**, 520–523 (2013).
51. Li, X. et al. Mechanochromic and conductive chiral nematic nanostructured film for bioinspired ionic skins. *ACS nano* **17**, 12829–12841 (2023).
52. Geng, Y., Kizhakidathazhath, R. & Lagerwall, J. P. F. Robust cholesteric liquid crystal elastomer fibres for mechanochromic textiles. *Nat. Mater.* **21**, 1441–1447 (2022).
53. Nguyen, H. K. et al. Insights into mechanical dynamics of nanoscale interfaces in epoxy composites using nanorheology atomic force microscopy. *ACS Appl. Mater. interfaces* **15**, 38029–38038 (2023).
54. Park, H. et al. Mechanochromic Palettes of Cholesteric Liquid Crystal Elastomers for Visual Signaling. *Advanced optical materials* **12**, n/a (2024).
55. Zhou, J., Tang, W., Arakawa, Y., Tsuji, H. & Aya, S. Viscoelastic properties of a thioether-based heliconical twist-bend nematogen. *Phys. Chem. Chem. Phys.* **22**, 9593–9599 (2020).
56. Mahyaoui, C. N., Davidson, P., Meyer, C. & Dozov, I. Polymerisation of twist-bend nematic textures for electro-optical applications. *Soft matter* **2**, 4859–4867 (2024).
57. Borshch, V. et al. Nematic twist-bend phase with nanoscale modulation of molecular orientation. *Nat. Commun.* **4**, 2635 (2013).
58. Bouligand, Y. Twisted fibrous arrangements in biological materials and cholesteric mesophases. *Tissue cell* **4**, 189–217 (1972).
59. Baklanova, K. D., Dolganov, V. K., Kats, E. I. & Dolganov, P. V. Sequence of three-, two-, and one-dimensional structures formed from a cholesteric liquid crystal at change in the chirality. *Jetp Lett.* **117**, 535–539 (2023).
60. Bouligand, Y. Recherches sur les textures des états mésomorphes – 2. — Les champs polygonaux dans les cholestériques. *J. de Phys.* **33**, 715–736 (1972).
61. Jiajia Yang, W. eidongZ. hao, Zhou Yang, W. anliH. e, Jingxia Wang, T. omikil. keda & Lei Jiang, P. hotonicS. hapeM. emory Polymer Based on Liquid Crystalline Blue Phase Films. *ACS Appl. Mater. Interfaces* **11**, 46124–46131 (2019).
62. Natarajan, B. & Gilman, J. W. Bioinspired Bouligand cellulose nanocrystal composites: a review of mechanical properties. *Philos. Trans. R. Soc. A* **376**, 20–20170050 (2018).
63. Stewart, D. & Imrie, c. T. Synthesis and characterization of spin-labelled and spin-probed side-chain liquid crystal polymers. *Polym. (Guilford)* **37**, 3419–3425 (1996).
64. Alexander, G. P. & Yeomans, J. M. Numerical results for the blue phases. *Liq. Cryst.* **36**, 1215–1227 (2009).
65. Fournier, J. - & Galatola, P. Modeling planar degenerate wetting and anchoring in nematic liquid crystals. *Europhys. Lett.* **72**, 403–409 (2005).
66. Ravnik, M. & Žumer, S. Landau-de Gennes modelling of nematic liquid crystal colloids. *Liq. Cryst.* **36**, 1201–1214 (2009).
67. Hicks, A. L. & Walker, S. W. Modelling and simulation of the cholesteric landau-de gennes model. *Proc. R. Soc. A* **480**, 20230813 (2024).
68. Mori, H., Gartland, E. C. Jr, Kelly, J. R. & Bos, P. J. Multidimensional director modeling using the Q tensor representation in a liquid crystal cell and its application to the  $\pi$  cell with patterned electrodes. *Jpn. J. Appl. Phys.* **38**, 135–146 (1999).
69. Swain, J. & Tierra, G. Linear numerical schemes for a Q-tensor system for nematic liquid crystals. *Comput. Methods Appl. Mech. Eng.* **430**, 117190 (2024).
70. Hecht, F. New development in FreeFem. *J. Numer. Math.* **20**, 251–266 (2012).
71. Johnson, C. R., Hansen, C. D. & Johnson, C. R. Jr. Paraview: an end-user tool for large-data visualization. In *Visualization Handbook*, 717–731 (2005).

## Acknowledgements

This work was financially supported by the National Science Foundation DMR-2337740 (X.L., T.P., M.A., Y.W.). Work performed at the Center for Nanoscale Materials, a U.S. Department of Energy Office of Science User Facility, was supported by the U.S. DOE, Office of Basic Energy Sciences, under Contract No. DE-AC02-06CH11357. X.L. and T.P. thanks Ming Ye from Bruker for data collection and useful discussion on nanoDMA characterization. X.L. and T.P. acknowledge the use of the UNT Microscopy and Imaging Laboratory and the assistance of Andrea Bernardino with confocal characterization.

## Author contributions

X.L. conceived the study, designed the experiments and supervised the work. T.P., X.L., M.A. and Y.W. performed the experiments. G.T. conceived and designed the simulations. J.S. and G.T. performed the simulations. D.C. and R.D. contributed to chemical pattern fabrication. S.K. and Y.Y. contributed to the tensile test sample preparation. T.P., J.S., G.T. and X.L. wrote the manuscript. All authors discussed the results and contributed to data analysis and manuscript revision.

## Competing interests

The authors declare no competing interests.

## Additional information

**Supplementary information** The online version contains supplementary material available at <https://doi.org/10.1038/s41467-025-64332-y>.

**Correspondence** and requests for materials should be addressed to Xiao Li.

**Peer review information** *Nature Communications* thanks the anonymous reviewers for their contribution to the peer review of this work. A peer review file is available.

**Reprints and permissions information** is available at <http://www.nature.com/reprints>

**Publisher's note** Springer Nature remains neutral with regard to jurisdictional claims in published maps and institutional affiliations.

**Open Access** This article is licensed under a Creative Commons Attribution-NonCommercial-NoDerivatives 4.0 International License, which permits any non-commercial use, sharing, distribution and reproduction in any medium or format, as long as you give appropriate credit to the original author(s) and the source, provide a link to the Creative Commons licence, and indicate if you modified the licensed material. You do not have permission under this licence to share adapted material derived from this article or parts of it. The images or other third party material in this article are included in the article's Creative Commons licence, unless indicated otherwise in a credit line to the material. If material is not included in the article's Creative Commons licence and your intended use is not permitted by statutory regulation or exceeds the permitted use, you will need to obtain permission directly from the copyright holder. To view a copy of this licence, visit <http://creativecommons.org/licenses/by-nc-nd/4.0/>.

© The Author(s) 2025